DC Impedance Modeling and Design-Oriented Harmonic Stability Analysis of MMC-PCCF-Based HVDC System

Pengkun Li, *Graduate Student Member, IEEE*, Yue Wang, *Member, IEEE*, Xuan Li, *Member, IEEE*, Bo Yue, Runtian Li, Bole Feng, and Taiyuan Yin

***Abstract*—A modular multilevel converter with a passive circulating current filter (MMC-PCCF) is a novel topology that can inherently suppress circulating currents and has a lower modulation index penalty than the traditional MMC. However, the harmonic stability issue of the MMC-PCCF-based HVdc system is more complex, which has not been well addressed yet. This article, for the first time, develops accurate dc impedance models of MMC-PCCF in different control modes and compares them with that of the traditional MMC in a wide frequency range mathematically. It is revealed that more resonance points exist in MMC-PCCF, leading to higher harmonic instability risks. To comprehensively study the stability of the MMC-PCCF-based HVdc system, this article proposes a design-oriented harmonic stability analysis method based on resistance sensitivity and phase-difference sensitivity and sums up a guideline for the system stability improvement. Furthermore, this article also presents a more intuitive explanation of the leading cause for system harmonic instability. It is demonstrated that the proportional coefficient of the dc voltage controller behaves as a negative "resistance–inductance" at the dc side. Based on this new sight, two typical damping control methods are compared in terms of parameter design and dynamic performance. Finally, real-time hardware-in-the-loop results verify the theoretical analysis.**

***Index Terms*—Circulating current control, damping control, harmonic stability, impedance modeling, modular multilevel converter, phase-difference sensitivity, resistance sensitivity.**

ABBREVIATION

MMC	Modular multilevel converter.
HVdc	High-voltage direct current.
PCCF	Passive circulating current filter.
ACCSC	Active circulating current suppressing control.
HSS	Harmonic state-space.
SM	Submodule.
CM	Common mode.
DM	Differential mode.
PLL	Phase-locked loop.
FD	Frequency-dependent.
SEMMC	Sending-end modular multilevel converter.
REMMC	Receiving-end modular multilevel converter.
MAF	Moving-average filter.

NOMENCLATURE

N	Number of SM in each arm.
C_{m}	SM capacitor.
L_0	Arm inductance of the traditional MMC.
r_L	Equivalent parasitic resistance of each arm.
L_1	Parallel inductance of PCCF.
L_2	Series inductance of PCCF.
C_0	Capacitance of PCCF.
ω_{s}	Series resonance frequency of PCCF.
ω_{p}	Parallel resonance frequency of PCCF.
ω_1	Fundamental angular frequency.
m_{au}	Modulation index of phase *a* upper arm.
i_{au}	Current of phase *a* upper arm.
i_{au_c}	CM components of i_{au}.
i_{au_d}	DM components of i_{au}.
v_{au}	Sum of SM capacitor voltages in phase *a* upper arm.
C	Equivalent SM capacitance of each arm.
$\lvert\cdot\rvert$	Absolute value of a scalar variable.
d	Length of dc cable.
L_{sm1}	Smoothing reactor at dc port of SEMMC.
L_{sm2}	Smoothing reactor at dc port of REMMC.

Manuscript received June 8, 2021; revised September 28, 2021; accepted November 12, 2021. Date of publication November 22, 2021; date of current version December 31, 2021. This work was supported by the Science and Technology Projects of State Grid Corporation of China under Grant 5100-202056393A-0-0-00. Recommended for publication by Associate Editor D. G. Xu. (*Corresponding author: Yue Wang*.)

Pengkun Li, Yue Wang, Runtian Li, Bole Feng, and Taiyuan Yin are with the State Key Laboratory of Electrical Insulation and Power Equipment, Xi'an Jiaotong University, Xi'an 710049, China (e-mail: lipengkun@stu.xjtu.edu.cn; davidwangyue@mail.xjtu.edu.cn; runtianli1998@stu.xjtu.edu.cn; fengbl@stu.xjtu.edu.cn; yintaiyuan945@126.com).

Xuan Li and Bo Yue are with the State Grid Economic and Technological Research Institute Co., Ltd., Beijing 102209, China (e-mail: lixuan@chinasperi.sgcc.com.cn; yuebo2000@163.com).

Color versions of one or more figures in this article are available at https://doi.org/10.1109/TPEL.2021.3129471.

Digital Object Identifier 10.1109/TPEL.2021.3129471

I. INTRODUCTION

OVER the past decade, modular multilevel converter (MMC) has attracted more and more attention due to excellent features [1], e.g., high modularity, voltage scalability, and low voltage distortion. These features make MMC a promising solution in high- and medium-voltage applications, such as high-voltage direct current (HVdc) transmission systems, solid-state transformers, and railway static power conditioners. In the traditional MMC topology, as shown in Fig. 1(a) [2], the modulation index penalty may exceed 9%, and abundant voltage and power capacity are wasted [3]. In 2010, ABB Corporation

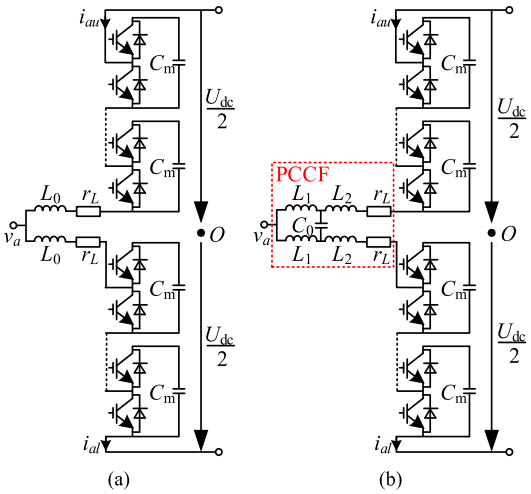

Fig. 1. Single-phase diagrams of (a) traditional MMC and (b) MMC-PCCF.

proposed MMC with passive circulating current filter (MMC-PCCF), as shown in Fig. 1(b), for HVdc transmission [4], and the problem of modulation index penalty does not exist in this novel topology. Besides, ABB Corporation has applied MMC-PCCF in many practical projects [5], such as Dolwin 2.

MMC-PCCF can inherently suppress second-order circulating current harmonics by its particular power-stage circuit and does not need additional active circulating current suppressing control (ACCSC), such as the traditional MMC. Thus, this novel topology has zero modulation index penalty owing to the inexistence of the second-order frequency modulation index [3]. Therefore, compared with the traditional MMC, MMC-PCCF needs fewer submodules (SMs) and smaller SM capacitance values, and then, the weight and cost of MMC-PCCF-based converter stations can also be reduced to a certain extent.

Despite the advantages mentioned above, the harmonic stability issue in MMC-PCCF-based HVdc systems is still severe. With several resonance instability accidents that occurred in practical HVdc projects, this issue has become increasingly prominent. When analyzing the harmonic stability issue of interconnected systems, the impedance-based method is a very effective approach [6]. To obtain accurate mathematical impedance models, the harmonic state-space (HSS) method and multiharmonic linearization method are commonly used in multi-frequency systems [7]–[9], and these two methods are mathematical equivalent essentially [10].

In the harmonic stability analysis of MMC-based systems, many scholars have conducted in-depth research works, and the key work is to establish accurate ac and dc impedance models.

For ac impedance modeling, Lyu *et al.* [11]–[17] established ac impedance models of the traditional MMC considering internal dynamics in multiple control modes based on the HSS method and multiharmonic linearization method. The influence of control parameters and time delay on the ac impedance of the traditional MMC was also analyzed in [18]–[20]. Wu emphatically studied the stability of the traditional MMC when feeding linear ac systems and analyzed the effects of zero-sequence circulating current control [21]–[23]. As for MMC-PCCF, most literature only focuses on its power and voltage penalty [24]–[28] but rarely conducts its impedance modeling and stability analysis. Scholars in Idaho National Laboratory and ABB Corporation developed ac impedance models of MMC-PCCF and analyzed system harmonic stability when it feeds grid or renewable energy sources [29]. However, delta-to-star transformation in PCCF complicated the power-stage modeling, and phase current control was also ignored.

For dc impedance modeling, Ji and Wang developed dc impedance models of the traditional MMC in multiple control modes [30]–[34]. The shaping of dc admittance was also studied [35]. Nevertheless, the influences of smoothing reactors and long-distance dc cables have not been thoroughly discussed.

Until now, dc impedance modeling and stability analysis of the MMC-PCCF-based HVdc system has not been well addressed and needs further analysis, which is thus the focus of this article. Besides the complex couplings in bridge arms similar to the traditional MMC, PCCF, which is connected between upper and lower arms, makes the impedance modeling of MMC-PCCF more complicated [36], [37]. Moreover, the following three important problems have not been addressed in previous impedance-based stability analyses.

1) *Lack of theoretical basis to divide HVdc system into two subsystems*: The prerequisite in impedance-based stability analysis method is ensuring the stability of subsystems. However, when dividing the whole system into two subsystems, most studies combine the passive dc network with a random converter station as a subsystem without considering its stability analysis. The theoretical division basis and subsystem stability analysis are crucial and could not be neglected, particularly when the multiple π, or multiple T, or frequency-dependent (FD) dc network model is adopted.
2) *Lack of quantitative parameter influence analysis*: In the eigenvalue-based stability analysis method, the participation-factor method is adopted to evaluate the influence of parameters quantitatively. However, no corresponding systematic approach exists in the impedance-based stability analysis method [38]–[40]. Some literature works tried to establish a frequency-domain sensitivity analysis methodology to identify parameters in complex power systems and evaluate the influence degree of parameters [41]–[44]. So far, very few papers have touched on the application of frequency-domain sensitivity in the design of system harmonic stability. And the only existing research mainly focused on the eigenvalue sensitivity. Besides, the definition of impedance sensitivity is still not uniform, and the difference between the base values of different parameters is not taken into account, making the comparison of parameter sensitivity meaningless.
3) *Lack of a more intuitive explanation on the main cause for HVdc system instability*: Current studies have concluded that the proportional coefficient of dc voltage controller will cause negative damping to the HVdc system [32], [33], [45], [46], but they always attribute the negative

damping to the bandwidth of dc voltage control, which is not intuitive enough.

To cope with the above issues, the main contributions of this article are summarized as follows.

1) Without using complex circuit conversion, the power-stage model of MMC-PCCF is built by analyzing the flowing paths of different components of arm currents. Furthermore, accurate dc impedance models of MMC-PCCF in ac and dc voltage control modes are developed for the first time. In addition, the similarities and differences between the dc impedance of MMC-PCCF and the traditional MMC in a wide frequency range are explicitly revealed.
2) A design-oriented harmonic stability analysis method based on resistance sensitivity and phase-difference sensitivity is proposed, and a guideline is summed up for improving harmonic stability of the MMC-PCCF-based HVdc system. The proposed method and guideline are also adapted to general interconnected systems.
3) A more intuitive explanation of the leading cause for the dc-side harmonic instability of the MMC-PCCF-based HVdc system is clarified. Based on this new sight, a comparative study of two damping control methods is carried out in terms of parameter design and dynamic performance. And the obtained conclusions are also applicable for any other dc systems with dc-voltage-controlled converters.

The rest of this article is organized as follows. Section II presents the power-stage scheme and steady-state modeling of MMC-PCCF. Section III derives dc impedance models of MMC-PCCF and reveals the similarities and differences between dc impedance of MMC-PCCF and the traditional MMC. Design-oriented harmonic stability analysis of the MMC-PCCF-based HVdc system is carried out in Section IV. Section V presents a new sight at the damping control. Section VI gives the real-time hardware-in-the-loop (HIL) experimental results. Finally, Section VII concludes this article.

II. Power-Stage Scheme and Steady-State Modeling of MMC-PCCF

This section introduces the power-stage scheme of MMC-PCCF, especially the parameter design of PCCF, and elaborates on the steady-state modeling of the power stage, in which complex internal dynamics and multiple harmonics are taken into account. Unlike the traditional MMC, the passive filter in MMC-PCCF complicates the power stage and significantly affects the port impedance. To overcome the modeling difficulties brought by PCCF, flowing paths of different components of arm currents are emphatically analyzed, avoiding complex circuit conversion, such as delta–star transformation.

A. Power-Stage Scheme

Fig. 1(b) shows the single-phase diagram of MMC-PCCF, and the three phases are symmetrical. Each phase has an upper arm and a lower arm, and each arm consists of N SMs. All SMs adopt the half-bridge topology in this article. C_{m} is the capacitance value of SM capacitors and r_L is the equivalent parasitic resistance of each arm. L_1 and L_2 are arm inductors and C_0 is connected in parallel with two L_1 to form the PCCF. One worth mentioning is that the sum of L_1 and L_2 satisfies

$$L_1 + L_2 = L_0 \tag{1}$$

to have the same transient and steady-state performances as the traditional MMC shown in Fig. 1(a), where L_0 is the arm inductor of the traditional MMC. Filter impedance for common-mode (CM) components of arm currents is

$$Z(j\omega) = 2r_L + j\frac{2\omega(L_1+L_2) - 4\omega^3 L_1 L_2 C_0}{1 - 2\omega^2 L_1 C_0} \tag{2}$$

where one series resonance point and one parallel resonance point exist and corresponding resonance frequencies are

$$\omega_{\mathrm{s}} = \sqrt{\frac{L_1+L_2}{2L_1L_2C_0}} \tag{3}$$

$$\omega_{\mathrm{p}} = \sqrt{\frac{1}{2L_1C_0}} \tag{4}$$

where ω_{s} and ω_{p} are, respectively, the series and parallel resonance frequencies of PCCF. To suppress circulating currents at second-order frequency, ω_{p} must be selected as $2\omega_1$, where ω_1 is the fundamental angular frequency. To avoid amplifying any other CM components of arm currents, ω_{s} could be an odd-order frequency, such as $3\omega_1$, $5\omega_1$, and so on. In summary, once the series resonance frequency and L_0 are determined, L_1, L_2, and C_0 could be solved and obtained accordingly.

B. Steady-State Modeling

Electrical variables in Fig. 1(b) are represented with two subscripts, respectively, designating the phase (*a*, *b*, and *c*) and the arm (*u* means upper arm and *l* means lower arm). In terms of steady-state characteristics of MMC-PCCF, insertion indices of upper and lower arms only contain components at dc and fundamental frequency. Currents at dc and fundamental frequency flow through SMs and are coupled with modulation indices, causing dc, fundamental, and second-order harmonics in SM capacitor voltages. Then, capacitor voltages are coupled with modulation indices again, causing higher frequency harmonics in output arm voltages and arm currents, which will be again circularly coupled with insertion indices. It is found that the coupling process is similar to the traditional MMC. The difference is that the absence of insertion index with second-order frequency reduces the third-order harmonics in SM capacitor voltages compared with the traditional MMC, as shown in the contrastive case study in Table I.

Before establishing the steady-state model, two assumptions are provided. 1) Balancing algorithm of SM capacitor voltages works perfectly; thus, all SM capacitor voltages are equal to each other, which does not affect the dynamics of converter below switching frequency. This is also a common assumption of current studies. 2) Harmonics above Nyquist frequency are ignored; thus, the averaged model is adopted and the impedance model developed in the following is effective below the Nyquist frequency, which is similar to the traditional MMC.

TABLE I
HARMONIC COMPONENTS OF THE SUM OF SM CAPACITOR VOLTAGES IN PHASE A UPPER ARM

Harmonic Components	DC	Base	2nd	3rd
MMC-PCCF	4.985e5	2.437e4	1.031e4	1.568
The traditional MMC	4.982e5	2.448e4	1.034e4	318.8

Note: Two MMCs work under the same steady-state condition, including transmission power, port voltages, and currents.

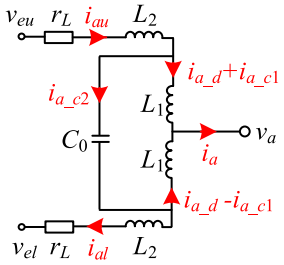

Fig. 2. Diagram of PCCF in phase a.

Another problem is that the parallel capacitor C_0 is connected between the upper and lower arms, so it is not easy to just model a single arm. Here, the flowing paths of CM and differential mode (DM) components of arm currents need further analysis. As shown in Fig. 2, CM currents flow through $r_{\rm L}$ and L_2, and then are shunted in the filter. But all DM currents flow through $r_{\rm L}$, L_2, and L_1, and then are output to the ac side.

Thus, the time-domain model of phase a upper arm is represented as

$$r_L i_{au} + L_2 \frac{di_{au}}{dt} + L_1 \frac{di_{a\_c1} + di_{a\_d}}{dt} = \frac{U_{\rm dc}}{2} - v_a - m_{au} v_{au} + v_n \tag{5}$$

$$C \frac{dv_{au}}{dt} = m_{au} i_{au} \tag{6}$$

where m_{au} and i_{au} are, respectively, insertion index and current of phase a upper arm. v_a is the ac-side terminal voltage of phase a. v_{au} is the sum of SM capacitor voltages in phase a upper arm, and $C = C_{\rm m}/N$ is the equivalent SM capacitance of each arm. i_{a_d} and i_{a_c} are, respectively, DM and CM components of i_{au}

$$i_{au} = i_{a\_c} + i_{a\_d}. \tag{7}$$

i_{a_c1} and i_{a_c2} are two parts of i_{a_c} and are expressed as

$$i_{a\_c1} = i_{a\_c} \cdot \frac{Z_{c\_pccf}}{Z_{l\_pccf} + Z_{c\_pccf}} \tag{8}$$

$$i_{a\_c2} = i_{a\_c} - i_{a\_c1} \tag{9}$$

where

$$Z_{l\_pccf} = 2j\omega L_1 \tag{10}$$

$$Z_{c\_pccf} = \frac{1}{j\omega C_0} \tag{11}$$

where ω is the angular frequency of i_{a_c}.

$v_{\rm n}$ in (5) represents the voltage difference from the floating middle point of the dc bus to the ac neutral, which can be expressed by (12) [16]. Notably, this formula includes state variables in phase b and phase c. To express the power-stage model using a single arm, $v_{\rm n}$ should be eliminated, which will be expanded in detail in the next section.

$$v_n = \frac{1}{6} \sum_{x=a,b,c} (m_{xl} v_{xl} - m_{xu} v_{xu}). \tag{12}$$

Due to the complex coupling of electrical variables in SMs, a series of harmonics are generated. Thus, each electrical variable in the power-stage averaged model contains multiple components in different frequencies. But amplitudes of high-frequency components are extremely small and could be ignored. Harmonics within the third order are considered in the modeling of this article and the modeling accuracy can be guaranteed [16], [34]. Taking variables in phase a upper arm as an example, complex vectors of these variables can be expressed as

$$\begin{cases} \boldsymbol{v}_{\rm dc} = \left[0\ 0\ 0\ U_{\rm dc}\ 0\ 0\ 0\right]^T \\ \boldsymbol{v}_a = \left[0\ 0\ 0.5V_{a1}e^{-j\varphi_1}\ 0\ 0.5V_{a1}e^{j\varphi_1}\ 0\ 0\right]^T \\ \boldsymbol{i}_{au} = \left[0\ 0\ 0.5I_{au1}e^{-j\alpha_1}\ I_{au0}\ 0.5I_{au1}e^{j\alpha_1}\ 0\ 0\right]^T \\ \boldsymbol{m}_{au} = \\ \left[0.5M_{au3}e^{-j\beta_3}\ 0.5M_{au2}e^{-j\beta_2}\ 0.5M_{au1}e^{-j\beta_1}\ M_{au0}\right. \\ \quad \left. 0.5M_{au1}e^{j\beta_1}\ 0.5M_{au2}e^{j\beta_2}\ 0.5M_{au3}e^{j\beta_3}\right]^T \\ \boldsymbol{v}_{au} = \left[0.5V_{au3}e^{-j\gamma_3}\ 0.5V_{au2}e^{-j\gamma_2}\ 0.5V_{au1}e^{-j\gamma_1}\ V_{au0}\right. \\ \quad \left. 0.5V_{au1}e^{j\gamma_1}\ 0.5V_{au2}e^{j\gamma_2}\ 0.5V_{au3}e^{j\gamma_3}\right]^T \\ \boldsymbol{v}_n = \left[0.5V_{n3}e^{-j\phi_3}\ 0.5V_{n2}e^{-j\phi_2}\ 0.5V_{n1}e^{-j\phi_1}\ V_{n0}\right. \\ \quad \left. 0.5V_{n1}e^{j\phi_1}\ 0.5V_{n2}e^{j\phi_2}\ 0.5V_{n3}e^{j\phi_3}\right]^T. \end{cases} \tag{13}$$

Take $\boldsymbol{m}_{au}$ as an example. M_{auk} (k = 0, 1, 2, 3) and $\beta_{\rm k}$ are, respectively, amplitude and phase of the kth-order harmonic component of $m_{\rm au}$. Other symbols have similar meanings, thus are not repeated here.

Hence, time-domain averaged model (5) and (6) can be transformed to the frequency domain and expressed as

$$\boldsymbol{Z}_l \boldsymbol{i}_{au} = \frac{\boldsymbol{v}_{\rm dc}}{2} - \boldsymbol{v}_a - \boldsymbol{m}_{au} \otimes \boldsymbol{v}_{au} + \boldsymbol{v}_n \tag{14}$$

$$\boldsymbol{Y}_c \boldsymbol{v}_{au} = \boldsymbol{m}_{au} \otimes \boldsymbol{i}_{au} \tag{15}$$

where $\otimes$ is the symbol of convolution. $\boldsymbol{Z}_l$ and $\boldsymbol{Y}_c$ are the diagonal matrices representing impedance of arm inductor and admittance of equivalent SM capacitor and are expressed as

$$\boldsymbol{Z}_l = \text{diag}\left[Z_{l-3}\ Z_{l-2}\ Z_{l-1}\ Z_{l0}\ Z_{l+1}\ Z_{l+2}\ Z_{l+3}\right] \tag{16}$$

$$\boldsymbol{Y}_c = j2\pi C \cdot \text{diag}\left[-3f_1\ -2f_1\ -f_1\ 0\ f_1\ 2f_1\ 3f_1\right] \tag{17}$$

where

$$Z_{lk}=\begin{cases} j2k\pi f_1\left(L_1+L_2\right)+r_L, & k \text{ is odd} \\ j2k\pi f_1\left(L_2+L_1/\right. \\ \left.\left(1-2L_1C_0(2k\pi f_1)^2\right)\right)+r_L, & k \text{ is even}. \end{cases} \tag{18}$$

III. Sequence Impedance Modeling and Analysis

This section first develops the small-signal models of the power stage and control system of MMC-PCCF, then derives its accurate dc impedance models under ac and dc voltage control modes. Furthermore, to clarify the similarities and differences between MMC-PCCF and the traditional MMC, a detailed comparison between the dc impedance of these two topologies in a wide frequency range is illustrated.

A. Small-Signal Modeling of Power Stage

To obtain the dc impedance model of MMC, first, a sinusoidal voltage perturbation $\hat{v}_p$ with frequency f_p is added to the dc side, then the current response $\hat{i}_p$ with perturbation frequency is generated correspondingly. The dc impedance of MMC could be derived according to the ratio of $\hat{v}_p$ and $\hat{i}_p$. Here, dc voltage after disturbed is represented as

$$v_p=U_{\rm dc}+\hat{v}_p=U_{\rm dc}+V_p\cos(2\pi f_p t+\varphi_p) \tag{19}$$

where $\hat{v}_p$ is the dc voltage perturbation. V_p and φ_p are amplitude and initial phase of $\hat{v}_p$. Because the measurement of dc impedance is based on the obtained linear time-invariant system after linearization, it is independent of the initial phase angle of the voltage perturbation. To facilitate the calculation, the initial phase φ_p is set to zero.

Due to the symmetry of three phases, if dc impedance of phase *a* upper arm is derived, the whole dc impedance of MMC could be obtained according to the series and parallel connections of six arms. Hence, subscripts *a*, *b*, and *c* can be dropped in the following derivation to simplify the notation. When dc voltage perturbation is added to the dc side, strong couplings between steady-state and small-signal variables generate a series of small-signal harmonics with frequencies $f_p\pm k{\cdot}f_1$ (*k* is an integer). Harmonics caused by couplings between small signals could be ignored due to extremely small amplitudes. As mentioned before, steady-state harmonics within third-order frequency are considered, so the range of *k* is also no more than 3 for small-signal harmonics. Since voltage perturbation added to the dc side has symmetrical effects on three phases and six arms, the phase and sequence relationships of small-signal harmonics are expressed as

$$f=\begin{cases} f_p+3kf_1, & \text{zero sequence} \\ f_p+(3k+1)f_1, & \text{positive sequence} \\ f_p+(3k-1)f_1, & \text{negative sequence} \end{cases}$$

$$f=\begin{cases} f_p+(2k+1)f_1, & \text{differential mode} \\ f_p+2kf_1, & \text{common mode}. \end{cases} \tag{20}$$

According to the above analysis, after linearization of the averaged model (14) and (15), the power-stage small-signal model of MMC-PCCF can be derived as

$$\boldsymbol{Z}_l\hat{\boldsymbol{i}}_u=\frac{\hat{\boldsymbol{v}}_p}{2}-\hat{\boldsymbol{v}}_a-\boldsymbol{M}_u\hat{\boldsymbol{v}}_u-\boldsymbol{V}_u\hat{\boldsymbol{m}}_u+\hat{\boldsymbol{v}}_n \tag{21}$$

$$\boldsymbol{Y}_c\hat{v}_u=\boldsymbol{I}_u\hat{m}_u+\boldsymbol{M}_u\hat{i}_u \tag{22}$$

where $\hat{i}_u$, $\hat{m}_u$, and $\hat{v}_u$ are the vectors of small-signal harmonics, which are represented in the frequency domain as (23), where $\hat{I}_{p+k}$, $\hat{M}_{p+k}$, $\hat{V}_{p+k}$, and $\hat{\alpha}_{p+k}$, $\hat{\beta}_{p+k}$, $\hat{\gamma}_{p+k}$ ($k=0, \pm1, \pm2, \pm3$) are, respectively, the amplitude and phase of harmonic components of $\hat{i}_u$, $\hat{m}_u$, and $\hat{v}_u$ with frequency $f_{\rm p}+k{\cdot}f_1$.

$\boldsymbol{M}_{\rm u}$, $\boldsymbol{V}_{\rm u}$, and $\boldsymbol{I}_{\rm u}$ are Toeplitz matrices of steady-state electrical variables and have similar forms, which are expressed as (24) in a unified form, where X_k and δ_k ($k=0, 1, 2, 3$) are, respectively, the amplitude and phase of the *k*th-order harmonic component of *X*.

Similar to steady-state features, CM and DM components of small-signal arm currents have different flowing paths in PCCF. $\boldsymbol{Z}_l$ and $\boldsymbol{Y}_c$ are small-signal impedance of arm inductor and admittance of equivalent SM capacitor, which are, respectively, expressed as

$$\boldsymbol{Z}_l=\text{diag}\left[Z_{l-3}\quad Z_{l-2}\quad Z_{l-1}\quad Z_{l0}\quad Z_{l+1}\quad Z_{l+2}\quad Z_{l+3}\right] \tag{25}$$

$$\boldsymbol{Y}_c=j2\pi C\cdot\text{diag}\left[f_p{-}3f_1\quad f_p{-}2f_1\quad f_p{-}f_1\quad f_p\quad f_p{+}f_1\quad f_p{+}2f_1\quad f_p{+}3f_1\right] \tag{26}$$

where

$$Z_{lk}=\begin{cases} j2\pi\left(f_p+kf_1\right)\left(L_1+L_1\right)+r_L, & k \text{ is odd} \\ j2\pi\left(f_p+kf_1\right)\left(L_2+L_1/\right. \\ \left.\left(1-2L_1C_0(2\pi\left(f_p+kf_1\right))^2\right)\right)+r_L. & k \text{ is even}. \end{cases} \tag{27}$$

As shown in (12), $\hat{\boldsymbol{v}}_n$consists of variables in three phases, and to derive the dc impedance of phase *a* upper arm, it is necessary to eliminate variables of phases *b* and *c* in the power-stage model. Using the similar method in [16], first transform (21) into

$$\hat{\boldsymbol{i}}_{\rm u}=\boldsymbol{Y}_l\left(\hat{\boldsymbol{v}}_p/2-\hat{\boldsymbol{v}}_a-\boldsymbol{M}_u\hat{\boldsymbol{v}}_u-\boldsymbol{V}_u\hat{\boldsymbol{m}}_u+\hat{\boldsymbol{v}}_n\right) \tag{28}$$

where $\boldsymbol{Y}_l$ is the inverse of $\boldsymbol{Z}_l$. Then set elements in $\boldsymbol{Y}_l$ corresponding to DM zero-sequence components to zero. As a result, all elements in $\hat{i}_u$corresponding to DM zero-sequence components are forced to zero and $\hat{\boldsymbol{v}}_n$can be dropped without affecting the solution. According to the sequence and phase relationships in (20), small-signal harmonics with frequency $f_p{+}6k{+}3$ ($k=-1$, 0) are DM zero-sequence components. Therefore, the elements $\boldsymbol{Y}_l(1, 1)$ corresponding to the frequency of $f_{\rm p}{-}3f_1$ and $\boldsymbol{Y}_l(7, 7)$ corresponding to the frequency of $f_{\rm p}{+}3f_1$ are forced to be zero. Then $\boldsymbol{Y}_l$ is expressed as

$$\boldsymbol{Y}_l=\text{diag}\left[0\quad\frac{1}{Z_{l-2}}\quad\frac{1}{Z_{l-1}}\quad\frac{1}{Z_{l0}}\quad\frac{1}{Z_{l+1}}\quad\frac{1}{Z_{l+2}}\quad 0\right]. \tag{29}$$

After the modification and simplification, the power-stage small-signal model can be transformed into

$$\hat{\boldsymbol{i}}_u=\boldsymbol{Y}_l(\frac{\hat{\boldsymbol{v}}_p}{2}-\hat{\boldsymbol{v}}_a-\boldsymbol{M}_u\hat{\boldsymbol{v}}_u-\boldsymbol{V}_u\hat{\boldsymbol{m}}_u) \tag{30}$$

$$\boldsymbol{Y}_c\hat{\boldsymbol{v}}_u=\boldsymbol{I}_u\hat{\boldsymbol{m}}_u+\boldsymbol{M}_u\hat{\boldsymbol{i}}_u. \tag{31}$$

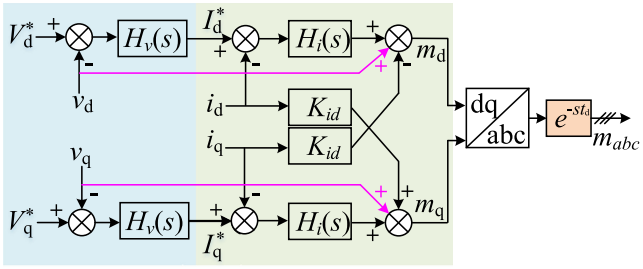

Fig. 3. Control diagram of MMC-PCCF in ac voltage control mode.

B. Small-Signal Modeling of Control System and Sequence Impedance in AC Voltage Control Mode

A block diagram of a typical dual-loop ac voltage control mode is shown in Fig. 3, including ac voltage control, phase current control, feedforward control, and time delay. In general, small-signal insertion index is the superposition of the above four control loops and can be modeled by

$$\hat{\boldsymbol{m}}_u = \boldsymbol{Q}_i \hat{\boldsymbol{i}}_u + \boldsymbol{P}_a \hat{\boldsymbol{v}}_a + \boldsymbol{P}_{feed} \hat{\boldsymbol{v}}_a \tag{32}$$

where effects of time delay are included in the other three coefficient matrices.

1) Phase Current Control: Phase current control mainly regulates the ac-side currents of three phases. Only DM components of arm currents that flow into the ac-side work on this control loop. Based on the sequence and phase relationships in (20), the coefficient matrix $\boldsymbol{Q}_i$ is expressed as

$$\boldsymbol{Q}_i = \mathrm{diag}[0\ 0\ a\ 0\ b\ 0\ 0] \tag{33}$$

where a (b) is the gain matrix of DM negative (positive) sequence small-signal harmonics with frequency $f_\mathrm{p}-f_1$ ($f_\mathrm{p}+f_1$) when compensated by regulars H_i(s) and K_{id}. Park transformation increases the frequency of DM negative-sequence components by f_1 and reduces the frequency of DM positive-sequence components by f_1; thus, a and b are expressed as

$$a = (H_i(j2\pi f_p) + jK_{id}) \cdot G_{\mathrm{d}1} \tag{34}$$

$$b = (H_i(j2\pi f_p) - jK_{id}) \cdot G_{\mathrm{d}2} \tag{35}$$

where $G_{\mathrm{d}1}$ and $G_{\mathrm{d}2}$ represents the effects of time delay on the transfer function matrix and are expressed as

$$G_{\mathrm{d}1} = e^{-j2\pi(f_p - f_1)\cdot t_\mathrm{d}} \tag{36}$$

$$G_{\mathrm{d}2} = e^{-j2\pi(f_p + f_1)\cdot t_\mathrm{d}}. \tag{37}$$

2) AC Voltage Control: Frequencies of small-signal ac voltage harmonics are f_p+f_1 and f_p-f_1; thus, $\boldsymbol{P}_a$ is expressed as

$$\boldsymbol{P}_a = \mathrm{diag}[0\ 0\ c\ 0\ d\ 0\ 0] \tag{38}$$

where

$$c = H_v(j2\pi f_p) H_i(j2\pi f_p) \cdot G_{\mathrm{d}1}/2 \tag{39}$$

$$d = H_v(j2\pi f_p) H_i(j2\pi f_p) \cdot G_{\mathrm{d}2}/2. \tag{40}$$

3) Feedforward Control: Like the ac voltage control loop, ac voltages are also directly fed to the insertion index. Thus, the gain matrix can be easily expressed as

$$\boldsymbol{P}_{feed} = \mathrm{diag}[0\ 0\ -0.5G_{\mathrm{d}1}\ 0\ -0.5G_{\mathrm{d}2}\ 0\ 0]. \tag{41}$$

In addition, relationships of small-signal voltages and currents of the ac-side load can be expressed as

$$\hat{v}_a = \boldsymbol{Z}_a \hat{i}_a = 2\boldsymbol{Z}_a \hat{i}_u \tag{42}$$

where $\boldsymbol{Z}_a$ is the small-signal impedance of the ac-side load and is expressed as

$$\boldsymbol{Z}_a = \mathrm{diag}[0\ 0\ z(f_p - f_1)\ 0\ z(f_p + f_1)\ 0\ 0]. \tag{43}$$

In summary, combining small-signal modeling of power stage and control system, the relationship between the small-signal current response of the upper arm and half of the voltage

$$\begin{cases} \hat{\boldsymbol{i}}_u = \big[0.5\hat{I}_{p-3}e^{j\hat{\alpha}_{p-3}}\ 0.5\hat{I}_{p-2}e^{j\hat{\alpha}_{p-2}}\ 0.5\hat{I}_{p-1}e^{j\hat{\alpha}_{p-1}}\ \hat{I}_{p0}e^{j\hat{\alpha}_p} \\ \quad 0.5\ \hat{I}_{p+1}e^{j\hat{\alpha}_{p+1}}\ 0.5\hat{I}_{p+2}e^{j\hat{\alpha}_{p+2}}\ 0.5\hat{I}_{p+3}e^{j\hat{\alpha}_{p+3}}\big]^T \\ \hat{\boldsymbol{m}}_u = \Big[0.5\hat{M}_{p-3}e^{j\hat{\beta}_{p-3}}\ 0.5\hat{M}_{p-2}e^{j\hat{\beta}_{p-2}}\ 0.5\hat{M}_{p-1}e^{j\hat{\beta}_{p-1}}\ \hat{M}_{p0}e^{j\hat{\beta}_p} \\ \quad 0.5\hat{M}_{p+1}e^{j\hat{\beta}_{p+1}}\ 0.5\hat{M}_{p+2}e^{j\hat{\beta}_{p+2}}\ 0.5\hat{M}_{p+3}e^{j\hat{\beta}_{p+3}}\Big]^T \\ \hat{\boldsymbol{v}}_u = \big[0.5\hat{V}_{p-3}e^{j\hat{\gamma}_{p-3}}\ 0.5\hat{V}_{p-2}e^{j\hat{\gamma}_{p-2}}\ 0.5\hat{V}_{p-1}e^{j\hat{\gamma}_{p-1}}\ \hat{V}_{p0}e^{j\hat{\gamma}_p} \\ \quad 0.5\ \hat{V}_{p+1}e^{j\hat{\gamma}_{p+1}}\ 0.5\hat{V}_{p+2}e^{j\hat{\gamma}_{p+2}}\ 0.5\hat{V}_{p+3}e^{j\hat{\gamma}_{p+3}}\big]^T \end{cases} \tag{23}$$

$$\boldsymbol{X}_u = \frac{1}{2}\begin{bmatrix} 2X_0 & X_1e^{-j\delta_1} & X_2e^{-j\delta_2} & X_3e^{-j\delta_3} & 0 & 0 & 0 \\ X_1e^{j\delta_1} & 2X_0 & X_1e^{-j\delta_1} & X_2e^{-j\delta_2} & X_3e^{-j\delta_3} & 0 & 0 \\ X_2e^{j\delta_2} & X_1e^{j\delta_1} & 2X_0 & X_1e^{-j\delta_1} & X_2e^{-j\delta_2} & X_3e^{-j\delta_3} & 0 \\ X_3e^{j\delta_3} & X_2e^{j\delta_2} & X_1e^{j\delta_1} & 2X_0 & X_1e^{-j\delta_1} & X_2e^{-j\delta_2} & X_3e^{-j\delta_3} \\ 0 & X_3e^{j\delta_3} & X_2e^{j\delta_2} & X_1e^{j\delta_1} & 2X_0 & X_1e^{-j\delta_1} & X_2e^{-j\delta_2} \\ 0 & 0 & X_3e^{j\delta_3} & X_2e^{j\delta_2} & X_1e^{j\delta_1} & 2X_0 & X_1e^{-j\delta_1} \\ 0 & 0 & 0 & X_3e^{j\delta_3} & X_2e^{j\delta_2} & X_1e^{j\delta_1} & 2X_0 \end{bmatrix} (\boldsymbol{X} = \boldsymbol{M}, \boldsymbol{V}, \boldsymbol{I}) \tag{24}$$

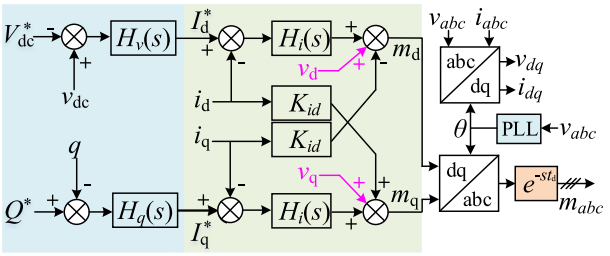

Fig. 4. Control diagram of MMC-PCCF in dc voltage control mode.

perturbation on the dc side is

$$\boldsymbol{Y}_p = [\boldsymbol{U} + \boldsymbol{Y}_l(\boldsymbol{M}_u\boldsymbol{Z}_c\boldsymbol{M}_u + 2\boldsymbol{Z}_a) + \boldsymbol{Y}_l(\boldsymbol{V}_u + \boldsymbol{M}_u\boldsymbol{Z}_c\boldsymbol{I}_u)(\boldsymbol{Q}_i + 2(\boldsymbol{P}_a + \boldsymbol{P}_{feed})\boldsymbol{Z}_a)]^{-1}\boldsymbol{Y}_l \tag{44}$$

where $\boldsymbol{Z}_c$ is the inverse of $\boldsymbol{Y}_c$. Hence, the dc impedance model of MMC-PCCF in ac voltage control mode is

$$Z_{\mathrm{dc\_MMC}}(f_p) = \frac{\hat{v}_p(f_p)}{\hat{i}_p(f_p)} = \frac{2}{3\boldsymbol{Y}_p(4,4)}. \tag{45}$$

C. Small-Signal Modeling of Control System and Sequence Impedance in DC Voltage Control Mode

A block diagram of a typical dual-loop dc voltage control mode is shown in Fig. 4, including phase current control, dc voltage control, reactive power control, feedforward control, phase-locked loop (PLL), and time delay. In general, small-signal insertion index is the superposition of the above six control loops and can be modeled by

$$\hat{m}_u = \boldsymbol{Q}_i\hat{\boldsymbol{i}}_u - \boldsymbol{P}_d\hat{\boldsymbol{v}}_p/2 + \boldsymbol{P}_q\hat{\boldsymbol{i}}_u + \boldsymbol{P}_{feed}\hat{\boldsymbol{v}}_a + \boldsymbol{P}_{pll}\hat{\boldsymbol{v}}_a \tag{46}$$

where effects of time delay are included in the other five coefficient matrices.

1) Phase Current Control: This control loop works in the same way as that in ac voltage control mode; thus, the coefficient matrix $\boldsymbol{Q}_i$ is easily derived as

$$\boldsymbol{Q}_i = \mathrm{diag}[0\ 0\ a\ 0\ b\ 0\ 0] \tag{47}$$

where

$$a = (H_i(j2\pi f_p) + jK_{id}) \cdot G_{\mathrm{d1}} \tag{48}$$

$$b = (H_i(j2\pi f_p) - jK_{id}) \cdot G_{\mathrm{d2}}. \tag{49}$$

2) DC Voltage Control: The frequency of small-signal dc voltage harmonics is f_p; thus, $\boldsymbol{P}_d$ is expressed as

$$\boldsymbol{P}_d(:,4) = \begin{bmatrix}0\ 0\ g\ 0\ h\ 0\ 0\end{bmatrix}^T \tag{50}$$

where g (h) is the gain matrix of CM zero-sequence small-signal harmonics with frequency f_{p}. But the small-signal insertion indices generated by this control loop are with frequencies $f_{\mathrm{p}}+f_1$ and f_{p}-f_1 due to asymmetric inverse Park transformation. And the amplitude is halved. Thus, g and h are expressed as

$$g = -H_v(j2\pi f_p)H_i(j2\pi f_p)G_{\mathrm{d1}}/2 \tag{51}$$

$$h = -H_v(j2\pi f_p)H_i(j2\pi f_p)G_{\mathrm{d1}}/2. \tag{52}$$

3) Reactive Power Control: In the steady state, reactive power is expressed as

$$q = 1.5\left(v_q \cdot i_d - v_d \cdot i_q\right). \tag{53}$$

Since the q-axis component of steady-state ac-side terminal voltages is zero, small-signal harmonics of reactive power can be simplified as

$$\hat{q} = 1.5\left(I_d \cdot \hat{v}_q - V_d \cdot \hat{i}_q - I_q \cdot \hat{v}_d\right). \tag{54}$$

The derivation is similar to the dc impedance modeling in the power control mode in [34], which will not go into detail here. The gain matrix is straightly expressed as

$$\boldsymbol{P}_q = 1.5\left(I_d\boldsymbol{P}_1\boldsymbol{Z}_{\boldsymbol{a}} - V_d\boldsymbol{P}_1 - I_q\boldsymbol{P}_2\boldsymbol{Z}_{\boldsymbol{a}}\right) \tag{55}$$

where

$$\boldsymbol{P}_1 = \begin{bmatrix} 0\ 0 & 0 & 0 & 0 & 0\ 0 \\ 0\ 0 & 0 & 0 & 0 & 0\ 0 \\ 0\ 0 & m\cdot G_{\mathrm{d1}} & 0 & -m\cdot G_{\mathrm{d1}} & 0\ 0 \\ 0\ 0 & 0 & 0 & 0 & 0\ 0 \\ 0\ 0 & -m\cdot G_{\mathrm{d2}} & 0 & m\cdot G_{\mathrm{d2}} & 0\ 0 \\ 0\ 0 & 0 & 0 & 0 & 0\ 0 \\ 0\ 0 & 0 & 0 & 0 & 0\ 0 \end{bmatrix} \tag{56}$$

$$\boldsymbol{P}_2 = \begin{bmatrix} 0\ 0 & 0 & 0 & 0 & 0\ 0 \\ 0\ 0 & 0 & 0 & 0 & 0\ 0 \\ 0\ 0 & -jm\cdot G_{\mathrm{d1}} & 0 & -jm\cdot G_{\mathrm{d1}} & 0\ 0 \\ 0\ 0 & 0 & 0 & 0 & 0\ 0 \\ 0\ 0 & jm\cdot G_{\mathrm{d2}} & 0 & jm\cdot G_{\mathrm{d2}} & 0\ 0 \\ 0\ 0 & 0 & 0 & 0 & 0\ 0 \\ 0\ 0 & 0 & 0 & 0 & 0\ 0 \end{bmatrix} \tag{57}$$

$$m = 0.5H_q(j2\pi f_p)H_i(j2\pi f_p). \tag{58}$$

4) Feedforward Control: Similar to the derivation in ac voltage control mode, the gain matrix is

$$\boldsymbol{P}_{feed} = \mathrm{diag}[0\ 0\ -0.5G_{\mathrm{d1}}\ 0\ -0.5G_{\mathrm{d2}}\ 0\ 0]. \tag{59}$$

5) Phase-Locked Loop: Small-signal ac voltage harmonics bring disturbance to the phases locked by PLL. Thus, all segments containing Park or inverse Park transformation will be

$$\boldsymbol{P}_{pll} = \begin{bmatrix} 0\ 0 & 0 & 0 & 0 & 0\ 0 \\ 0\ 0 & 0 & 0 & 0 & 0\ 0 \\ 0\ 0 & (A_1+A_2+A_3+A_4)\cdot G_{\mathrm{d1}} & 0 & (B_1+B_2+B_3+B_4)\cdot G_{\mathrm{d1}} & 0\ 0 \\ 0\ 0 & 0 & 0 & 0 & 0\ 0 \\ 0\ 0 & (C_1+C_2+C_3+C_4)\cdot G_{\mathrm{d2}} & 0 & (D_1+D_2+D_3+D_4)\cdot G_{\mathrm{d2}} & 0\ 0 \\ 0\ 0 & 0 & 0 & 0 & 0\ 0 \\ 0\ 0 & 0 & 0 & 0 & 0\ 0 \end{bmatrix} \tag{60}$$

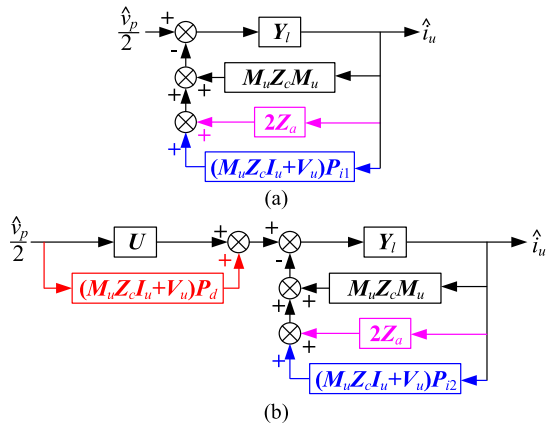

Fig. 5. Block diagrams of dc impedance of MMC-PCCF in (a) ac voltage control mode and (b) dc voltage control mode.

influenced, including the above four control loops. The derivation process is similar but is more complex and comprehensive than that in [34]. The gain matrix is as (60) which is shown here straightly due to the space limitation where

$$A_1 = -B_1 = 0.5G_\theta(\mathrm{j}2\pi f_p)\cdot(-\boldsymbol{I}_u^*(H_i(\mathrm{j}2\pi f_p)+\mathrm{j}K_{id})+\boldsymbol{M}_u^*)$$
$$C_1 = -D_1 = 0.5G_\theta(\mathrm{j}2\pi f_p)(-\boldsymbol{M}_u+\boldsymbol{I}_u(H_i(\mathrm{j}2\pi f_p)+\mathrm{j}K_{id})) \quad (61)$$

$$A_2 = -B_2 = -C_2 = D_2 = -\frac{3}{8}I_d V_1 H_q(j2\pi f_p)H_i(j2\pi f_p)G_\theta(j2\pi f_p) \quad (62)$$

$$A_3 = -B_3 = -C_3 = D_3 = \frac{3}{8}V_d I_1\cos(\varphi_z)H_q(j2\pi f_p)H_i(j2\pi f_p)G_\theta(j2\pi f_p) \quad (63)$$

$$A_4 = -B_4 = -C_4 = D_4 = \frac{1}{4}V_1 G_\theta(j2\pi f_p). \quad (64)$$

Then, the relationship between the small-signal current response of the upper arm and half of the voltage perturbation on the dc side is

$$\begin{aligned}\boldsymbol{Y}_p = (&\boldsymbol{U}+2\boldsymbol{Y}_l\boldsymbol{Z}_a+\boldsymbol{Y}_l\boldsymbol{M}_u\boldsymbol{Z}_c\boldsymbol{M}_u\\&+\boldsymbol{Y}_l(\boldsymbol{M}_u\boldsymbol{Z}_c\boldsymbol{I}_u+\boldsymbol{V}_u)(\boldsymbol{Q}_i+\boldsymbol{P}_q\\&+\boldsymbol{P}_{feed}\boldsymbol{Z}_a+2\boldsymbol{P}_{pll}\boldsymbol{Z}_a))^{-1}\boldsymbol{Y}_l(\boldsymbol{U}\\&+(\boldsymbol{M}_u\boldsymbol{Z}_c\boldsymbol{I}_u+\boldsymbol{V}_u)\boldsymbol{P}_d).\end{aligned} \quad (65)$$

After substituting (65) into (45), the dc-side impedance model of MMC-PCCF in dc voltage control mode can be obtained.

Based on (44) and (65), the sequence models of MMC-PCCF in ac and dc voltage control modes can be equivalently presented in Fig.5, where the transfer matrices are defined as

$$\boldsymbol{P}_{i1} = \boldsymbol{Q}_i + 2(\boldsymbol{P}_a+\boldsymbol{P}_{feed})\boldsymbol{Z}_a \quad (66)$$

$$\boldsymbol{P}_{i2} = \boldsymbol{Q}_i + \boldsymbol{P}_q + \boldsymbol{P}_{feed}\boldsymbol{Z}_a + 2\boldsymbol{P}_{\mathrm{pll}}\boldsymbol{Z}_a. \quad (67)$$

In Fig. 5, black blocks represent the inherent open-loop features of MMC-PCCF. Purple blocks represent the coupling of dc- and ac-side impedances. Blocks marked in red and blue, respectively, represent the effects of dc voltage control loop and other control loops. Among all control loops, only the dc voltage control loop is in the position of feedforward, which implies that the effects of dc voltage control on dc impedance and system harmonic stability need special attention.

TABLE II
ELECTRICAL PARAMETERS OF MMC-PCCF

Parameter	AC Voltage Control	DC Voltage Control
Rated AC Voltage (V_{grms})	290 kV	290 kV
Rated DC Voltage (V_{dc})	500 kV	500 kV
Rated Power (P)	750 MW	750 MW
Arm Parasitic Resistance (r_L)	0.3 Ω	0.3 Ω
SM Capacitance (C_{m})	8 mF	8 mF
Number of SM/arm (N)	244	244
Arm Inductance (L_2)	44.44 mH	44.44 mH
Arm Inductance (L_1)	55.56 mH	55.56 mH
Capacitance of PCCF (C_0)	22.8 μF	22.8 μF
AC Side Load	0.02 H	0.05 H
Time Delay (t_{d})	150 μs	150 μs

TABLE III
CONTROL PARAMETERS OF MMC-PCCF

AC Voltage Control Mode			
Control Loop	Proportional Coefficient	Integral Coefficient	Decoupling Coefficient
Phase Current Control	0.5	8	4.459×10^{-4}
AC Voltage Control	5	400	N/A
DC Voltage Control Mode			
Control Loop	Proportional Coefficient	Integral Coefficient	Decoupling Coefficient
Phase Current Control	0.6	8	4.459×10^{-4}
DC Voltage Control	5	500	N/A
Reactive Power Control	0.1	100	N/A
PLL	180	3200	N/A

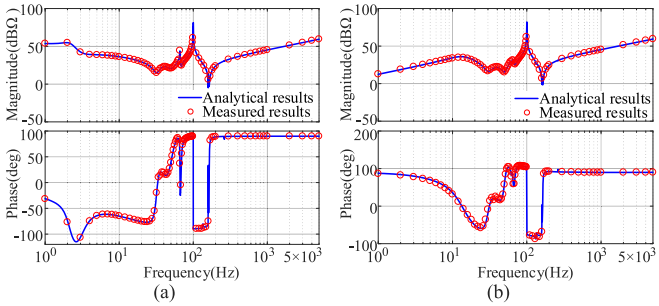

Fig. 6. Impedance response of MMC-PCCF in (a) ac voltage control mode and (b) dc voltage control mode.

D. Verification of the Proposed DC Impedance Models

To verify the correctness and accuracy of the proposed impedance models, detailed time-domain simulation models of MMC-PCCF in ac and dc voltage control modes are separately established in MATLAB/Simulink. Electrical parameters and per-unit control parameters are listed in Tables II and III. Here, series resonance frequencies of PCCFs are all set as $3\omega_1$ as an example. Impedance measured results are obtained by the frequency sweeping method. It is demonstrated from impedance curves, as shown in Fig. 6 that analytical and measured results

TABLE IV
CONTROL PARAMETERS OF ACCSC

Control Mode	Proportional Coefficient	Integral Coefficient	Decoupling Coefficient
AC Voltage Control	100	1000	31.416
DC Voltage Control	250	1000	31.416

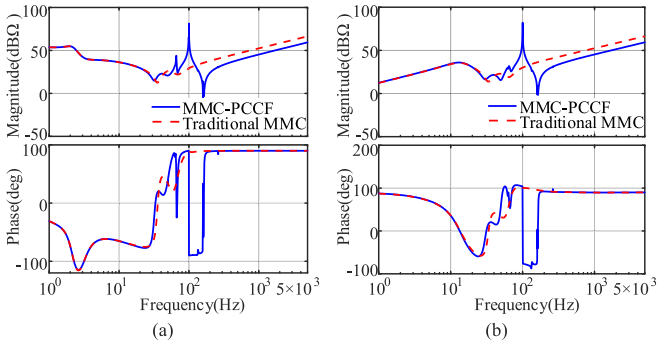

Fig. 7. Impedance response comparison of MMC-PCCF and the traditional MMC in (a) ac voltage control mode and (b) dc voltage control mode.

match well over the entire frequency range, which validates the correctness and accuracy of the derived dc impedance models of MMC-PCCF in ac and dc voltage control modes. From dc impedance curves, it is found that there are two obvious resonance points in amplitude–frequency characteristic curves: one resonance peak and one resonance valley. Two phase steps also exist in the phase–frequency curves correspondingly: one phase drop and one phase jump, whose frequencies are equal to that of resonance peak and valley, respectively. It is also shown in Fig. 6(b) that multiple negative-resistance frequency bands exist, which may bring instability risks to the MMC-PCCF-based HVdc system.

E. DC Impedance Comparison Between MMC-PCCF and the Traditional MMC

To clarify the peculiarity of MMC dc-side impedance brought by different circulating current suppressing control methods, this section will give a detailed impedance comparison of MMC-PCCF and the traditional MMC. To compare effectively, the same steady-state conditions are guaranteed, including insertion indices with the fundamental frequency, ac- and dc-side terminal voltages, currents, and transmission power. All electrical and control parameters are also equal except for the capacitance in PCCF and control parameters of ACCSC listed in Table IV. The dc impedance models of the traditional MMC are obtained by the same derivation procedures as MMC-PCCF, and the impedance curves of these two types of MMC schemes under different control modes are drawn in Fig. 7.

It can be noted that the differences are mainly reflected in the middle- and high-frequency ranges. Taking dc voltage control mode as an example, root causes for these distinctions in different frequency bands are as follows.

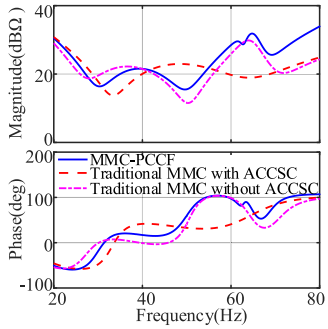

Fig. 8. Impedance curves of MMC-PCCF and the traditional MMC in the low-frequency band.

1) Low-Frequency Band (20–80 Hz): It is worth noting that the negative-resistance feature appears in impedance of MMC-PCCF but does not in the traditional MMC. This negative-resistance feature is caused by the proportional coefficient of dc voltage controller and is suppressed to a certain extent by ACCSC because the proportional and decoupling coefficients of ACCSC are equivalent to virtual arm resistors [36], [47]. But the bandwidth of PCCF is very narrow and has a little effect within this frequency band. As shown in Fig. 8, blue lines are impedance curves of MMC-PCCF. Red dashed lines and purple dot-dash lines are respectively impedance curves of the traditional MMC with and without ACCSC. It is indicated that when circulating currents are not suppressed in the traditional MMC, negative-resistance features also exist within 20–80 Hz such as MMC-PCCF, which verifies the above analysis.

2) Middle-Frequency Band (90–200 Hz): A prominent feature in this band is the resonance peak and valley in the amplitude–frequency curve of MMC-PCCF, and the two phase steps exist correspondingly in the phase–frequency curve. The resonance peak is caused by the parallel resonance of PCCF, which is located strictly at 100 Hz. The resonance valley is caused by the series resonance of PCCF but is also affected by SM capacitors and the control system. Thus, the frequency is not precisely designed 150 Hz. If ignoring complex coupling in SMs and control system, open-loop dc impedance model $Z_{\rm ol}$ of MMC-PCCF can be simplified as

$$Z_{\rm eq} = \frac{2}{3}\left(sL_2 + \frac{1}{2sC_0 + 1/sL_1} + \frac{N}{4sC_{\rm m}} + r_L\right). \quad (68)$$

As SM capacitance increases, couplings in SMs are weakened. Fig. 9(a) shows the open-loop impedance curves of MMC-PCCF $Z_{\rm ol}$ and simplified impedance model $Z_{\rm eq}$ with different SM capacitance. It is inferred that when SM capacitance is large enough (300 mF), the curve of $Z_{\rm ol}$ is consistent with that of $Z_{\rm eq}$, and the resonance valley is almost at 150 Hz, which verifies the correctness of the above analysis.

If different series resonance frequencies of PCCF are chosen, as shown in Fig. 9(b), the resonance valley will move correspondingly. One worth mentioning is that the negative-resistance feature is also weakened in this frequency band, which will reduce the oscillation risks.

3) High-Frequency Band (300–5000 Hz): It can be seen that in the high-frequency range, the impedance of MMC-PCCF and

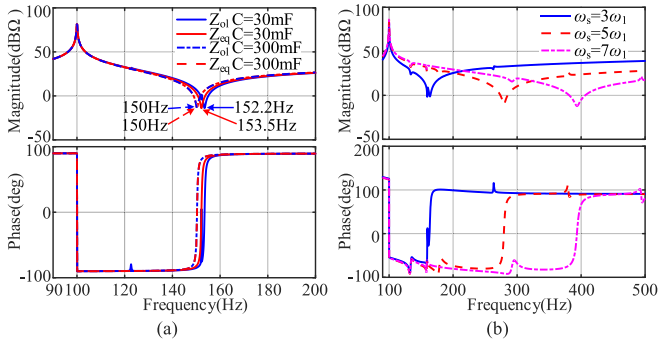

Fig. 9. Curves of (a) Z_{ol} and Z_{eq} with different SM capacitances and (b) closed-loop impedance with different series resonance frequencies of PCCF in the middle-frequency band.

the traditional MMC are both almost pure inductive but have different amplitudes. Here, the control system is ignored because it has a little effect within the high-frequency range. Open-loop impedance models of MMC-PCCF and the traditional MMC can, respectively, be simplified as

$$Z_{ol\_\mathrm{PCCF}} = \frac{2}{3}\left(\frac{1}{4C}\left(\frac{4|M_1|^2}{s-j2\pi f_1}+\frac{1}{s}+\frac{4|M_1|^2}{s+j2\pi f_1}\right) + r_L + sL_2 + \frac{sL_1}{1+2L_1C_0s^2}\right) \tag{69}$$

$$Z_{ol\_\mathrm{ACCSC}} = \frac{2}{3}\left(\frac{1}{4C}\left(\frac{4|M_1|^2}{s-j2\pi f_1}+\frac{1}{s}+\frac{4|M_1|^2}{s+j2\pi f_1}\right) + r_L + sL_2 + sL_1\right) \tag{70}$$

where M_1 is the amplitude of fundamental frequency insertion index of phase a upper arm. It is evident that in the high-frequency range, the impedances of both MMCs are almost pure inductive, and the impedance amplitude of the traditional MMC is a little larger than that of MMC-PCCF.

Synthesizing the above analysis, PCCF and ACCSC have the same suppressing effect on circulating currents but have different impacts on small-signal dc impedance in a wide frequency range. PCCF has a limited negative-resistance suppression function and brings more resonance points than ACCSC, which increases the resonance risks of the HVdc system.

IV. Design-Oriented Harmonic Stability Analysis of MMC-PCCF-Based HVDC System

Based on the built dc impedance models, this section comprehensively analyzes the port characteristics of MMC-PCCF and dc side harmonic stability of the MMC-PCCF-based HVdc system. To evaluate the effects of parameters qualitatively and quantitatively, this section applies frequency-domain sensitivity to impedance-based stability analysis and proposes a design-oriented harmonic stability analysis method based on resistance sensitivity and phase-difference sensitivity. Finally, a guideline is summed up for improving harmonic stability of the MMC-PCCF-based HVdc system.

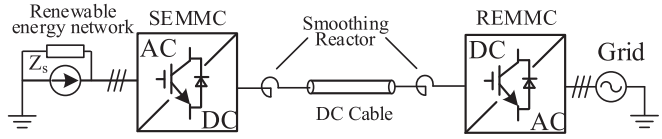

Fig. 10. Configuration of MMC-PCCF-based HVdc system.

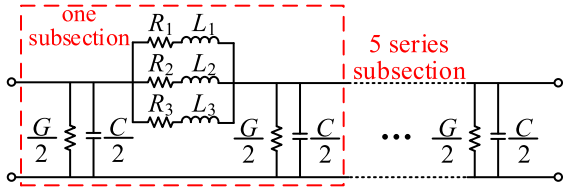

Fig. 11. FD dc cable model.

TABLE V
Parameters of DC Cable

Symbol	Value	Unit	Symbol	Value	Unit
r_1	0.1265	Ω/km	l_1	0.2644	mH/km
r_2	0.1504	Ω/km	l_2	7.2865	mH/km
r_3	0.0178	Ω/km	l_3	3.6198	mH/km
c	0.546	μF/km	g	0.1015	μS/km

A. Configuration of HVDC System and DC Cable Model

The diagram of an MMC-PCCF-based two-terminal HVdc transmission system is shown in Fig. 10, including dc-voltage-controlled and ac-voltage-controlled MMC stations, long dc cable, and smoothing reactors. Sending-end MMC (SEMMC) operates in ac voltage control mode, and receiving-end MMC (REMMC) operates in dc voltage control mode.

There are many types of dc cable models, such as resistance–inductance model, single or multiple π model, single or multiple T model, and FD model [48]–[50]. Most studies adopt the resistance–inductance model or single π model to simplify the analysis, which is inaccurate for long-distance cable and in high-frequency ranges. To better represent the dc-side stability characteristics, the FD dc cable model proposed by Beerten is adopted here [50]. The equivalent model of dc cable used in this study is shown in Fig. 11, which consists of five series subsections and three parallel *RL* branches in each subsection to reproduce cable electromagnetic transient behavior accurately and account for hyperbolic correction factors, improving cable model accuracy for long-distance and high-frequency ranges. Cable parameters are listed in Table V.

The renewable energy network impedance is presented as follows, which consists of cable impedance plus subnetwork impedance representing transformers, filter inductors, and other devices in the network [29]:

$$Z_s = 1.0894 + 30\mathrm{e}^{-3}j\omega\,(\Omega)\,. \tag{71}$$

B. Resistance Sensitivity of SEMMC and REMMC

Before applying the impedance-based stability criterion, the MMC-PCCF-based HVdc system needs to be divided into two subsystems, and the stability of these two subsystems needs to be guaranteed. However, to be precise, as shown in Fig. 12, the

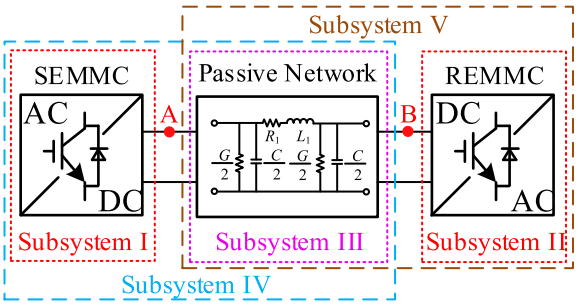

Fig. 12. Division diagram of MMC-PCCF-based HVdc system.

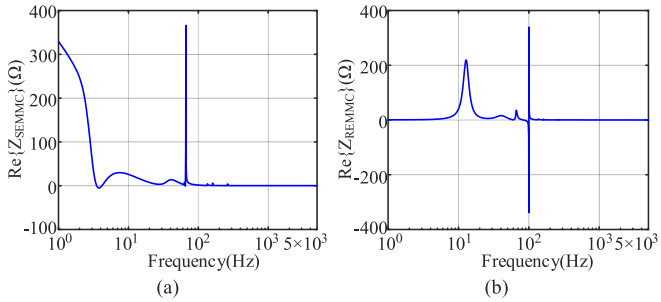

Fig. 13. Real parts of dc impedance of (a) SEMMC and (b) REMMC.

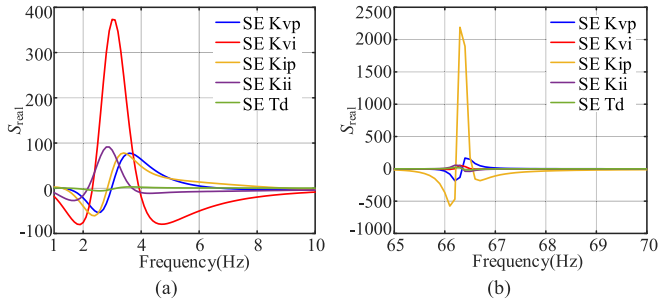

Fig. 14. Resistance sensitivities of control parameters of SEMMC within (a) 1–10 Hz and (b) 65–70 Hz.

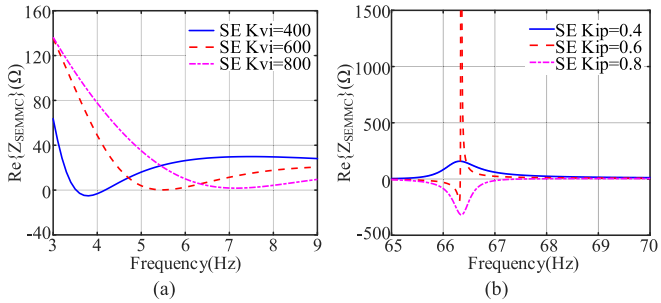

Fig. 15. Effects of (a) SE Kvi and (b) SE Kip on non-dissipative regions of SEMMC.

MMC-PCCF-based HVdc system can be divided into three cascaded subsystems. The first subsystem is SEMMC. The second is REMMC. The third subsystem is the passive network, including dc cable and smoothing reactors near two MMC stations. When these three subsystems are linked together, harmonic instability may occur at either port A or port B due to insufficient damping.

There are two methods to divide the whole system into two subsystems. The first way is to divide from port A. The segmentation result is that one is subsystem I, and the other is subsystem V consisting of subsystems II and III. The second way is to divide from port B. The segmentation result is that one is subsystem IV consisting of subsystems I and III, and the other is subsystem II. The focus of this matter is which MMC station should the passive network forms a new subsystem with. And no matter which division method is selected, a new interconnected system between an active converter subsystem and a passive network subsystem is formed, such as subsystems IV and V.

To select the division method and facilitate the harmonic stability analysis and design of the whole HVdc system, dc impedance characteristics of SEMMC and REMMC are first analyzed. To quantitatively evaluate the influence of control parameters, the resistance sensitivity is defined as

$$S_{\text{real}}(p,f) = \frac{\text{real}\left(Z\left(p'_0 + kp'_0\right)\right) - \text{real}\left(Z\left(p'_0\right)\right)}{kp'_0} = \frac{\text{real}\left(Z\left(p_0 + kp_0\right)\right) - \text{real}\left(Z\left(p_0\right)\right)}{k} \tag{72}$$

where $p' = p/p_0$. p_0 is the original parameter value and k is the perturbation percentage of p_0. In general, the range of k is about 5%–10%. Since there is no negative resistance in the passive network, the resistance sensitivity can be used to evaluate the oscillation risks when an active converter is connected with pure passive networks. More specifically, there is no nondissipative region in the impedance of pure passive network [51]; thus, only MMC converters could bring negative damping and cause instability to the interconnected system. Here, the nondissipative region represents the frequency band where the real parts of the impedance are negative [52].

Fig. 13 presents the real parts of the dc impedance of SEMMC and REMMC. It is shown in Fig. 13(a) that nondissipative regions appear within 1–10 Hz and 65–70 Hz. Therefore, these two frequency bands are focused on in the following resistance sensitivity study. Resistance sensitivities of control parameters, including proportional and integral coefficients of ac voltage control, phase current control, and time delay, are plotted in Fig. 14. If S_{real} is positive, it means that increasing this parameter can bring more positive damping to the system. It is indicated from the results that key parameters are the integral coefficient of ac voltage control, SE Kvi in 1–10 Hz, and the proportional coefficient of phase current control, SE Kip in 65–70 Hz. The effects of these two control parameters on nondissipative regions are plotted in Fig. 15. It is implied that in the range of 1–10 Hz, the nondissipative region is reduced with the increase of SE Kvi. In the range of 65–70 Hz, the nondissipative region is enlarged with the increase of SE Kip. Effects of other parameters could also be analyzed in the same way. To reduce oscillation risks, SE Kvi and SE Kip are separately modified to 800 and 0.4 in the following analysis, ensuring no nondissipative regions exist in the dc impedance of SEMMC.

It is shown in Fig. 13(b) that the nondissipative region mainly appears within 90–110 Hz. Resistance sensitivities of control

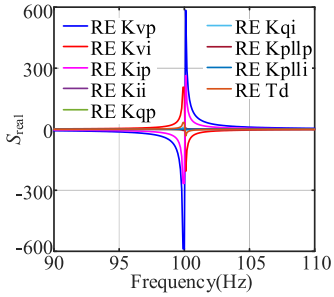

Fig. 16. Resistance sensitivities of control parameters of REMMC within 90–110 Hz.

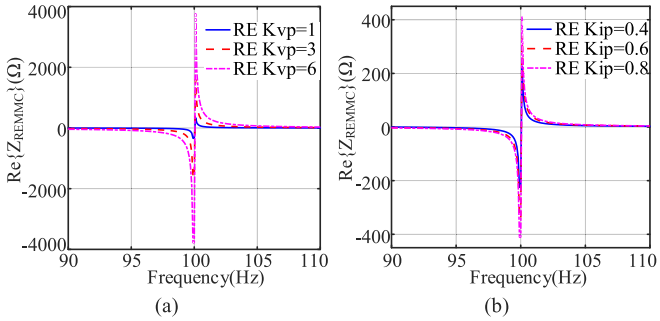

Fig. 17. Effects of (a) RE Kvp and (b) RE Kip on nondissipative regions of REMMC.

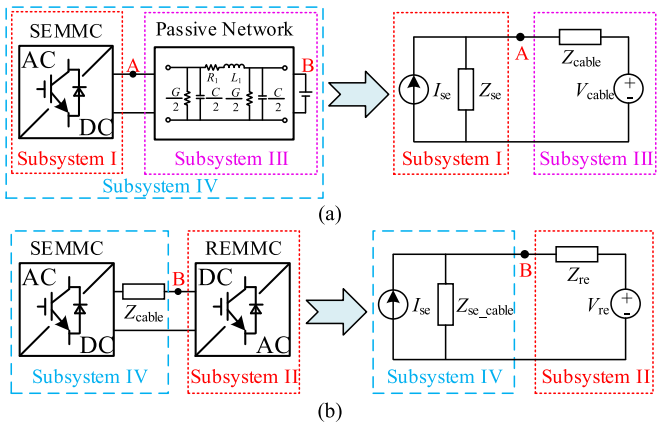

Fig. 18. Equivalent circuit of MMC-PCCF-based HVdc system. (a) Subsystem IV including SEMMC and passive network. (b) Whole HVdc system.

parameters are plotted in Fig. 16, which implies that key parameters are the proportional coefficients of dc voltage control and phase current control, respectively, RE Kvp and RE Kip. The effects of these two control parameters on nondissipative regions are plotted in Fig. 17. It is demonstrated that the nondissipative region is reduced with the decrease of RE Kvp and RE Kip. But the improvement effect brought by RE Kip is minimal. Effects of other parameters can also be analyzed similarly. To enhance system stability, RE Kvp is modified to 1 in the following system stability analysis.

According to the above analysis, it is demonstrated that the nondissipative regions in SEMMC can be eliminated by optimizing key parameters, while it is difficult to achieve that in REMMC. As shown in Fig. 18(a), when the dc side of subsystem

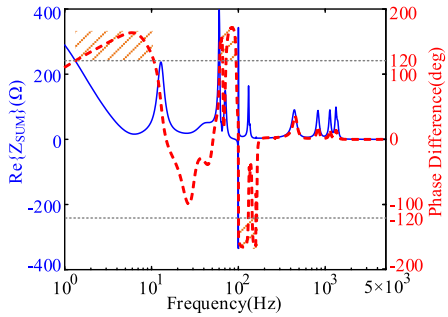

Fig. 19. Real-part sums and phase differences of the impedance of subsystems IV and II.

III is connected with an ideal dc voltage source, from the perspective of port A, subsystem I is equivalent to a current source subsystem, and subsystem III is equivalent to a voltage source subsystem. The stability of subsystem IV can be guaranteed due to the nonexistence of nondissipative regions in dc impedance of subsystems I and III. That is to say, the oscillation risks at port A of subsystem IV can be easily eliminated. Instability risks of the whole system mainly lie in port B. Thus, it is more appropriate to divide the whole system into two subsystems from port B and then focus on analyzing and designing the stability of port B of the whole system after ensuring the stability of subsystems IV and II. As shown in Fig. 18(b), from the perspective of port B, subsystem IV is equivalent to a current source subsystem, and subsystem II is equivalent to a voltage source subsystem.

C. Phase-Difference Sensitivity of HVDC System

After dividing the HVdc system into two subsystems from port B, the analysis focus becomes the interaction stability between two active subsystems. In this condition, resistance sensitivity is not suitable anymore because the stability is not directly related to the resistance sum of two subsystems, but the circles of the Nyquist curve going around $(-1, \mathrm{j}0)$ and right-half-plane poles of impedance ratio. Thus, the key index changes to the phase difference at intersection points of subsystem impedance bode plots. Based on this, similar to resistance sensitivity, phase-difference sensitivity is defined as follows to evaluate the influence of parameters quantitatively:

$$S_{\mathrm{pha-diff}}(p, f) = \frac{\arg\left(Z_{\mathrm{re}}\left(p_0 + kp_0\right)\right) - \arg\left(Z_{\mathrm{se\_cable}}\left(p_0 + kp_0\right)\right)}{k} - \frac{\arg\left(Z_{\mathrm{re}}\left(p_0\right)\right) - \arg\left(Z_{\mathrm{se\_cable}}\left(p_0\right)\right)}{k} \tag{73}$$

where Z_{re} is the dc impedance of REMMC and $Z_{\mathrm{se\_cable}}$ is the impedance sum of SEMMC, dc cable, and two smoothing reactors.

The resistance sum and phase difference of the two subsystems are plotted in Fig. 19. Although the real-part sum of two subsystem impedances is very small in the high-frequency range, the phase difference is also close to zero. Actually, instability is not easy to happen within this frequency range, which proves that resistance sensitivity is no longer a good stability index in

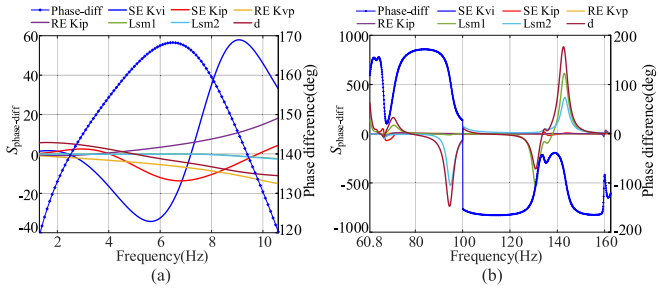

Fig. 20. Phase-difference sensitivities of main parameters in frequency ranges of (a) 1.3–10.6 Hz and (b) 60.8–162.6 Hz.

TABLE VI
RANKINGS OF PARAMETER SENSITIVITIES IN DIFFERENT FREQUENCY RANGES

Frequency Range	Key Parameters
1.3~10.6 Hz	SE Kvi >> SE Kip > RE Kip > RE Kvp > d
60.8~75 Hz	d > L_{sm1} > SE Kip > L_{sm2}
75~100 Hz	d > L_{sm2} >> L_{sm1} > RE Kvp > RE Kip
100~120 Hz	L_{sm2} > d >> RE Kvp > RE Kip
120~135 Hz	L_{sm1} > d >> L_{sm2}
135~162.6 Hz	d > L_{sm1} > L_{sm2} >> SE Kip

this condition. Besides, it is not appropriate to only study phase differences at intersection points of amplitude–frequency curves because if working conditions or parameter values change, the intersection points would also move accordingly. Therefore, here the absolute value of phase difference is defined as

$$\Delta_{\text{pha-diff}} = \left|\arg\left(Z_{\text{re}}\left(p_0\right)\right) - \arg\left(Z_{\text{se}}\left(p_0\right)\right)\right|. \tag{74}$$

As shown in Fig. 19, $\Delta_{\text{pha-diff}}$ in the pink shadow area exceeds 120°. This means that these regions have small phase margins and are more prone to instability, which makes them the focus of the subsequent research. In Fig. 19, $\Delta_{\text{pha-diff}}$ is above 120° within the frequency range of 1.3–10.6 Hz and 60.8–162.6 Hz. $S_{\text{pha-diff}}$ of dc cable length d, smoothing reactors, and key parameters studied in the last section are plotted in Fig. 20. d is set as 100 km here. L_{sm1} and L_{sm2} are, respectively, smoothing reactors near SEMMC and REMMC, which are both 50 mH. If $S_{\text{pha-diff}}$ is negative, it means that increasing this parameter can reduce phase difference and enlarge phase margin. The rankings of parameter sensitivities in different frequency ranges are given in Table VI. It is demonstrated that parameters have different influence degrees and rules in different frequency ranges. Corresponding parameters could be adjusted according to specific oscillation conditions, and Table VI could give a parameter optimization criterion for suppressing resonances. It is worth mentioning that there are many other constraint conditions for designing electrical and control parameters, such as cost, steady-state and dynamic performance, and so on; thus, the design of parameters needs to consider the compromise of these factors. For example, longer dc cables and larger smoothing reactors could improve system stability in some frequency bands, but the length of dc cables is decided by the transmission distance, and larger smoothing reactors will bring more cost and weight of converter stations. Therefore, optimizing control parameters is the first choice when improving system stability.

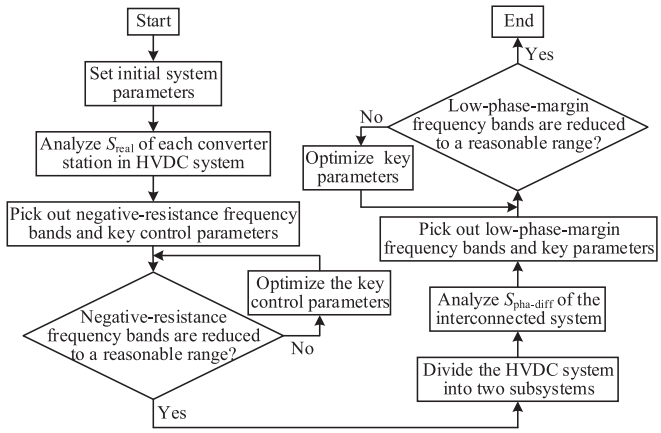

Fig. 21. Flowchart of the guideline for parameter optimization and harmonic stability improvement of MMC-PCCF-based HVdc system.

In conclusion, a guideline for system parameter optimization and harmonic stability improvement is proposed, as shown in Fig. 21. First, the negative-resistance frequency bands in each converter station are picked out and key control parameters are optimized based on resistance sensitivity. This provides a theoretical basis for dividing the whole system into two subsystems. Then, low-phase-margin frequency bands of the whole system are picked out and key system parameters are optimized based on phase-difference sensitivity. It is worth noting that when adjusting parameter values, the constraints from transient features, cost, and so on should also be taken into account, which is not the scope of this article, thus is not studied here. The proposed design-oriented harmonic stability analysis method and guideline are also applicable to the harmonic stability analysis of general interconnected systems.

Sometimes, negative-resistance frequency bands and low-phase-margin frequency bands can only be reduced to a reasonable range and cannot be eliminated entirely. In this condition, if the HVdc system is still unstable, some additional damping controls could be added to improve system stability, which will go into detail in Section V.

V. NEW SIGHT AT DAMPING CONTROL

To maintain the stability of the HVdc system, current studies always give a conservative method, which is to add damping control as much as possible, such as at both dc and ac sides and in each converter station [33], [45], [46]. But this is always redundant and will increase the control complexity. Section IV has revealed that the key to reducing the harmonic resonance risks at dc side of the MMC-PCCF-based HVdc system is to mitigate or eliminate the negative-resistance feature in the dc impedance of REMMC. In addition, according to the analysis in Section IV, it is the proportional coefficient of dc voltage controller, RE Kvp, which produces negative damping at dc port of REMMC and brings instability risks to the HVdc system. Existing studies always explain the negative damping from the bandwidth of dc voltage control, which is not intuitive enough. In contrast, this section will give a new sight at this proportional coefficient from the perspective of negative resistance and

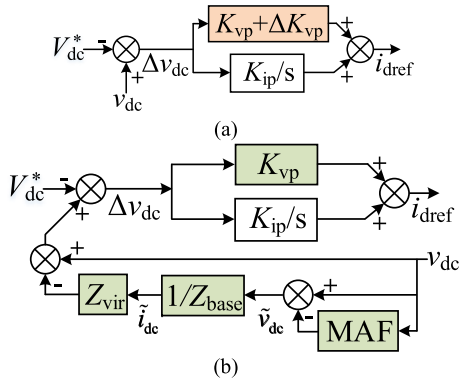

Fig. 22. Schematic diagram of (a) original form and (b) equivalent form of dc voltage control.

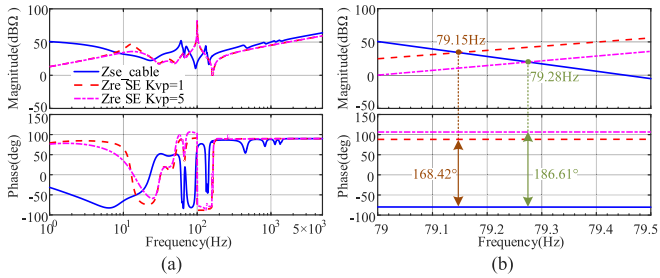

Fig. 23. Impedance curves of two subsystems of MMC-PCCF-based HVdc system. (a) Full scale. (b) Zoom-in figure.

compare two typical damping control methods applied to the MMC-PCCF-based HVdc system from the view of parameter design and dynamic performance.

A. New Sight at RE Kvp

Here we assume the PI controller of dc voltage control is

$$H_v(s) = K_{\rm vp} + \Delta K_{\rm vp} + \frac{K_{\rm vi}}{s} \tag{75}$$

where $K_{\rm vi}$ is the integral coefficient of the dc voltage controller.

And $K_{\rm vp}$ and $\Delta K_{\rm vp}$ are two parts of the proportional coefficient. The dc voltage control, as shown in Fig. 22(a), can be equivalently transformed to Fig. 22(b). $\tilde{v}_{dc}$ represents all the ac harmonics of $\tilde{v}_{dc}$, which is derived by a moving-average filter (MAF). $Z_{\rm vir}$ is expressed as

$$Z_{\rm vir} = -\Delta K_{\rm vp} Z_{\rm base} \frac{s}{k_p s + k_i} \tag{76}$$

where $Z_{\rm base}$ is defined as the nominal value of steady-state dc impedance for dimensional transformation.

If $\Delta K_{\rm vp}$ is positive, it means that a virtual negative "resistance–inductance" which acts on all harmonics in dc current is put at the dc side of REMMC, which explains more intuitively and simply that larger RE Kvp reduces the positive damping of REMMC. This conclusion is also valid for all dc-voltage-controlled converters, such as the traditional MMC and two-level voltage source converter.

Impedance curves of $Z_{\rm se\_cable}$ and $Z_{\rm re}$ are plotted in Fig. 23. It is shown that when RE Kvp increases from 1 to 5, the phase margin decreases from 11.58° to −6.61°, which indicates a potential harmonic resonance with a frequency of 79.28 Hz. According to the analysis in Section IV-C, the oscillation mode can also be eliminated by increasing d or $L_{\rm sm2}$, but this will increase the total cost, thus is uneconomical.

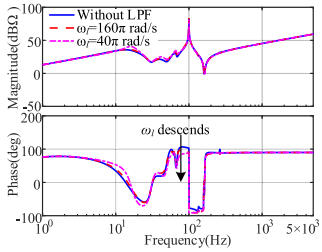

Fig. 24. Curves of the revised dc impedance of REMMC with different cutoff frequencies of LPF in method 1).

B. Comparison of Typical Damping Control Methods

Most damping strategies proposed to suppress dc-side harmonics can be unified by adding virtual resistance at different positions of MMC. Here, let us take filter in dc voltage control and active damping control, for example.

Method 1): *Filter in dc voltage control*: A low-pass filter (LPF) is added to RE Kvp and the transfer function of the dc voltage controller is written as

$$H_v^f(s) = K_{\rm vp}\frac{\omega_l}{s+\omega_l} + \frac{K_{\rm vi}}{s} \tag{77}$$

where ω_l is the cutoff frequency of the LPF. Comparing (77) and (75), it can be derived that

$$Z_{\rm vir} = K_{\rm vp} \cdot Z_{\rm base} \cdot \frac{s^2}{(s+\omega_l)(k_p s + k_i)}. \tag{78}$$

The real and imaginary parts of $Z_{\rm vir}$ can easily be both positive above 30 Hz by designing ω_l. Therefore, the LPF is equivalent to adding a positive resistance and inductance at the dc side of REMMC and reducing the negative resistance feature near 80 Hz. This method has similar effects as directly reducing $K_{\rm vp}$, and LPF is to further avoid influencing the steady state of REMMC. Especially, $Z_{\rm vir}$ is greatly decided by the value of $K_{\rm vp}$, which is a constraint factor in improving the function of LPF.

Substitute (77) into (51) and (52), then revised dc impedance model with additional damping control is derived. Impedance curves of REMMC with different ω_l are plotted in Fig. 24. It is shown that negative-resistance features of REMMC are greatly suppressed by LPF, and the lower the cutoff frequency is, the stronger the suppression effects are.

Method 2): *Active damping control*: The principle of this method is to add an increment to the original insertion index, which is related to the harmonics in dc current. This method is equivalent to injecting specific-order CM zero-sequence harmonics into bridge arms. This insertion index increment can be expressed as

$$\Delta m = \frac{i_{\rm dc}}{3} \cdot \frac{s}{s+\omega_h} \cdot R_{\rm vir} \tag{79}$$

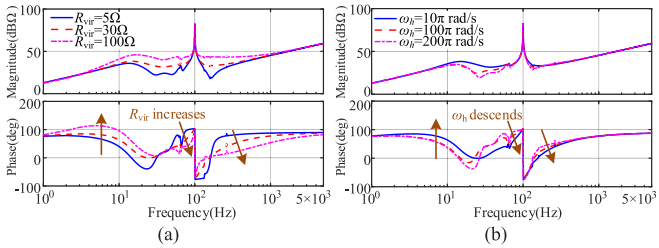

Fig. 25. Impedance curves of REMMC with different parameters of active damping control when (a) ω_h is fixed at 10π rad/s and (b) $R_{\rm vir}$ is fixed at 30 Ω.

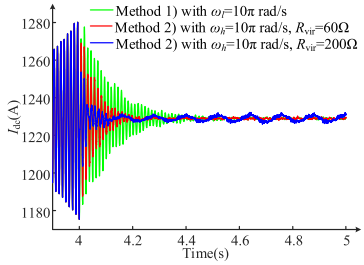

Fig. 26. DC current curves in method 1) and method 2) with different parameters.

where ω_h is the cutoff frequency of the high-pass filter (HPF). It is also equivalent to adding a positive resistance in bridge arms to suppress only the zero-sequence harmonics of arm currents if $R_{\rm vir}>0$; else, it is a negative resistance. The matrix of small-signal insertion index increment can be expressed as

$$\Delta\hat{\boldsymbol{m}}_u = \boldsymbol{Q}_{\rm damp}\hat{\boldsymbol{i}}_u \tag{80}$$

where

$$\boldsymbol{Q}_{\rm damp}= {\rm diag}\left[0\ 0\ 0\ \ \frac{s}{s+\omega_h}\cdot R_{\rm vir}\ 0\ 0\ 0\right]. \tag{81}$$

The revised dc impedance model could be derived by adding (80) to (46). DC impedance curves of REMMC with different parameters of active damping control are plotted in Fig. 25. It is shown in Fig. 25(a) that this method can effectively suppress the negative-resistance features of REMMC in the middle- and high-frequency ranges when $R_{\rm vir}>0$. It is worth mentioning that this strategy cannot eliminate the negative-resistance feature near 100 Hz but can effectively narrow the negative-resistance frequency band. It is also indicated that with the increase of $R_{\rm vir}$, impedance phases below 10 Hz increase and gradually exceed 90°, which proves that too large $R_{\rm vir}$ will cause lower frequency oscillations, as shown in simulation results in Fig. 26 (blue waveform). Thus, the value of $R_{\rm vir}$ has upper and lower boundaries. It is revealed in Fig. 25(b) that too large ω_h will weaken the suppression effects in the middle- and high-frequency ranges and ω_h has a smaller effect in the amplitude–frequency curve than $R_{\rm vir}$. Comparing Fig. 25(a) and (b), phase–frequency curves have a similar changing trend when $R_{\rm vir}$ increases and ω_h descends, which indicates that the design of $R_{\rm vir}$ and ω_h are coupled with each other. Generally, ω_h can be decided according to the actual oscillation frequency and R_{vir} can then be designed according to phase margin reflected in impedance curves.

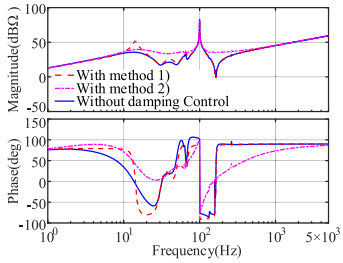

Fig. 27. Comparison of dc impedance of MMC-PCCF with and without damping control.

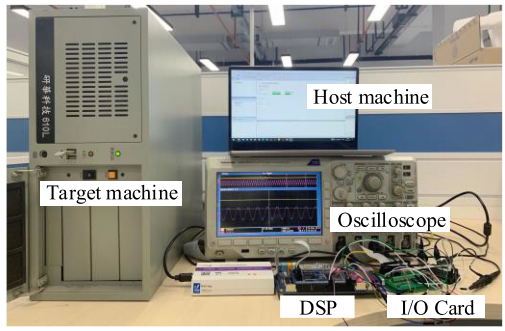

Fig. 28. Photograph of the HIL platform.

Besides, active damping control is a direct feedforward to insertion index and $R_{\rm vir}$ has higher design freedom; thus, this method could have a faster response with proper parameters than method 1) in suppressing oscillations, as shown in the green and red waveforms in Fig. 26.

Impedance curves of REMMC with and without damping control are shown in Fig. 27. Here, $\omega_l=\omega_h=10\pi$ rad/s and $R_{\rm vir}$ = 40 Ω. Notably, both damping control methods have a good effect in suppressing negative damping within the frequency band of 50–100 Hz. However, another nonnegligible impact is, phases within 1–15 Hz rise and approach 90° when method 1) or method 2) is applied, while the amplitudes are almost unchanged. This means that these two methods will reduce the system damping in the low-frequency band, and method 2) has a greater impact on the phase–frequency curve than method 1) within 9 Hz under the above parameters. Therefore, the design of damping control in practical engineering should consider this factor comprehensively to avoid seriously deteriorating the transient characteristics or causing other low-frequency oscillations.

VI. Experimental Verification

To further prove the effectiveness of proposed impedance models and theoretical analysis, a detailed real-time digital simulation model of the MMC-PCCF-based HVdc system, as shown in Fig. 10, is constructed in an HIL platform. The power-stage model of the HVdc system is emulated by the target machine, and the control system is realized through the DSP TMS320F28335 control board, as shown in Fig. 28. The system transmission power is set as 600 MW, and other parameters are adopted in Tables II–V and modified values in Section IV.

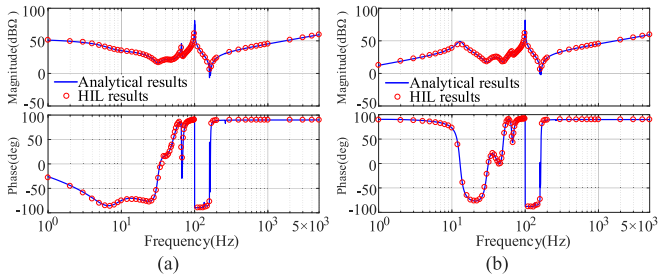

Fig. 29. Analytical and HIL results of dc impedance of (a) SEMMC and (b) REMMC.

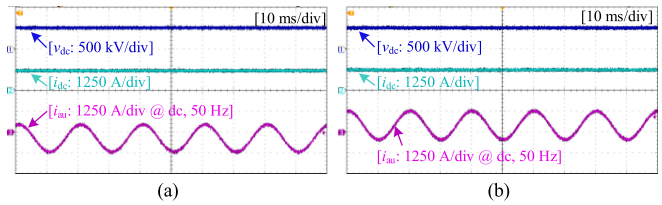

Fig. 30. Waveforms of dc voltages, dc currents, and arm currents of (a) Subsystem IV and (b) Subsystem II.

A. Verification of the Proposed DC Impedance Models

This section mainly verifies the proposed dc impedance models of MMC-PCCF in ac and dc voltage control modes. First, a voltage perturbation with frequency $f_{\rm p}$ is added to the dc side of SEMMC, then the current response with the perturbation frequency can be measured at the same port. The small-signal dc impedance value at frequency $f_{\rm p}$ is got by the ratio of voltage perturbation to current response. Sweeping frequency $f_{\rm p}$ from 1 Hz to 5 kHz, the small-signal dc impedance of SEMMC could be plotted in Fig. 29(a). DC impedance values of REMMC could be measured similarly and plotted in Fig. 29(b). It is found that the HIL results (circles) match well with the analytical results (solid lines), thus verifying the correctness of the proposed dc impedance models in Section III.

B. Stability Verification of Subsystems IV and II

To analyze the dc-side harmonic stability of the MMC-PCCF-based two-terminal HVdc system, the first step is to ensure the stability of two subsystems. Subsystem IV includes SEMMC, dc cable, and two smoothing reactors, and its dc side is connected with an ideal dc voltage source of 500 kV. Subsystem II includes REMMC alone and its dc side is connected with an ideal current source of 1200 A. Waveforms of dc port voltages, dc port currents, and arm currents of phase a upper arm in two MMCs are shown in Fig. 30. HIL results show that both two subsystems can work stably.

C. Harmonic Stability Analysis Verification of HVDC System

To verify the effectiveness of harmonic stability analysis, four cases are considered here. Case1): $d = 100$ km and $L_{\rm sm1} = L_{\rm sm2} = 50$ mH. Case 2): $d = 200$ km and $L_{\rm sm1} = L_{\rm sm2} = 50$ mH. Case 3): $d = 100$ km. $L_{\rm sm1} = 0.2$ H, and $L_{\rm sm2} = 50$ mH. Case 4): $d = 100$ km. $L_{\rm sm1} = 50$ mH, and $L_{\rm sm2} = 0.2$ H.

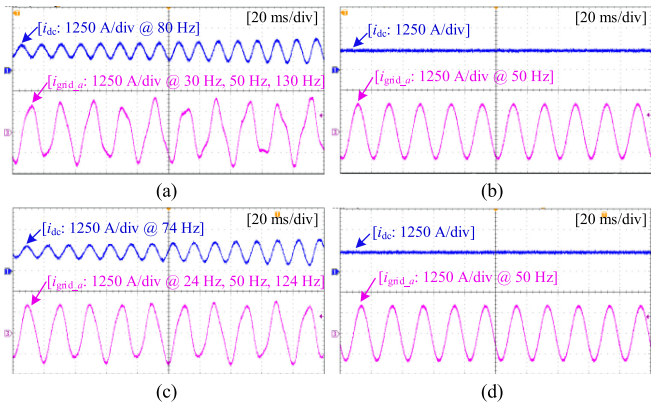

Fig. 31. Waveforms of dc currents and grid side currents in (a) Case 1), (b) Case 2), (c) Case 3), and (d) Case 4.

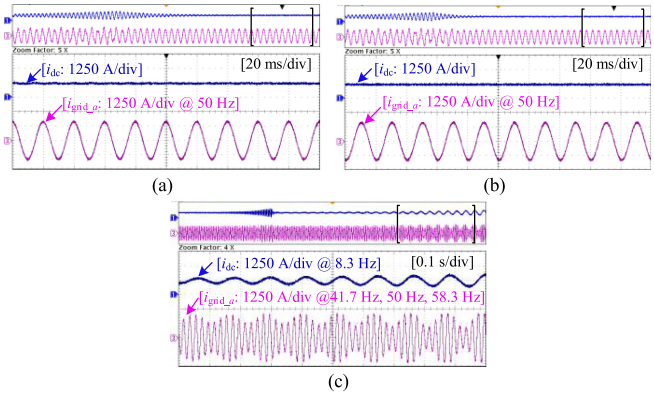

Fig. 32. Waveforms of dc currents and grid side currents in (a) Case 5), (b) Case 6), and (c) Case 7).

RE Kvp changes from 1 to 5 at 2.5 s and HIL results are presented in Fig. 31. It is indicated in Fig. 31(a) that when RE Kvp changes from 1 to 5, dc current begins to diverge and the system loses stability. The oscillation frequency is 80 Hz, which coincides with the analysis result in Section V-A. If the length of dc cable increases to 200 km, as shown in Fig. 31(b), the system will maintain stability, which verifies that longer dc cables could enhance the stability of HVdc system around 80 Hz. Comparison between Fig. 31(c) and (d) shows that increasing smoothing reactors near REMMC is more effective in enhancing system stability than that near SEMMC, which is also consistent with the previous analysis in Section IV-C.

D. Verification of Damping Control

MMC-PCCF-based HVdc system models with additional damping control are also built in the HIL platform. Three cases are considered here: Case 5): With the filter in dc voltage control. Case 6): With active damping control and $R_{\rm vir} = 60\,\Omega$. Case 7): With active damping control and $R_{\rm vir} = 200\,\Omega$. ω_l and ω_h are both 10π rad/s. HIL results shown in Fig. 32(a) and (b) verify the effectiveness of two damping control methods in suppressing resonances. Fig. 32(c) shows that when $R_{\rm vir}$ is too large, lower frequency oscillation is aroused at frequency 8.3 Hz verifying the correctness of analysis in Section V-B.

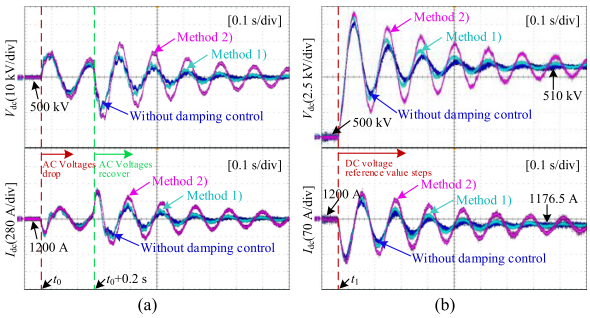

Fig. 33. Waveforms of voltages and currents at the dc port of REMMC in (a) Case 8) and (b) Case 9).

To further verify the effects of damping control on the transient characteristics of the MMC-PCCF-based HVdc system, two cases are mainly considered here: Case 8): ac-side voltage sag test; Case 9): step change test of dc voltage reference value. In two damping control methods, ω_l and ω_h are both 10π rad/s and $R_{\rm vir}$ equals 40 Ω. Waveforms of voltages and currents at the dc port of REMMC under two large-signal disturbances are shown in Fig. 33. In Case 8) as shown in Fig. 33(a), grid-side ac voltages drop to 0.7 per unit (p.u.) symmetrically at t_0 and recover to 1 p.u. after 0.2 s. In the process of convergence, the oscillation frequency is 7.5 Hz. In Case 9), as shown in Fig. 33(b), dc voltage reference value changes from 500 to 510 kV at t_1. In the process of convergence, the oscillation frequency is also 7.5 Hz. Both oscillation frequencies are within 9 Hz. The comparison between damping control and no damping control shows that the oscillation peaks are larger and the convergence rates are lower when damping controls are applied. It is confirmed that the positive damping of the MMC-PCCF-based HVdc system within 15 Hz is indeed reduced when method 1) or method 2) is applied. It is also shown that method 2) causes worse transient characteristics of the HVdc system than method 1) under the above parameters, which also verifies the theoretical analysis in Section V.

VII. Conclusion

This article develops accurate dc impedance models of MMC-PCCF in ac and dc voltage control modes and clarifies the similarities and differences between dc impedance of MMC-PCCF and the traditional MMC. It is revealed that PCCF has a limited negative-resistance suppression function and brings more resonance points, which may lead to higher instability risks.

This article presents the design-oriented harmonic stability analysis of the MMC-PCCF-based HVdc system based on resistance sensitivity and phase-difference sensitivity and then proposes a guideline. The influence of system parameters is studied quantitatively and key parameters are optimized to improve system stability. It is demonstrated that different key parameters dominate in different frequency bands, and corresponding parameters can be adjusted according to specific oscillation conditions.

This article also proposes a new sight at the damping control. It is demonstrated that the proportional coefficient of the dc voltage controller behaves as a negative "resistance–inductance" at the dc side. It is also unveiled that the filter in dc voltage control and active damping control are, respectively, equivalent to adding a positive harmonic resistance at the dc side and each bridge arm. Due to the direct feedforward to insertion index and higher parameter design freedom of active damping control, it could have a faster response speed than the other method in suppressing resonances.

According to the study of this article, MMC-PCCF can play a certain superiority in the conditions with relatively simple system architecture or high requirements for the weight and cost of converter stations, such as offshore HVdc systems. In complex power systems, MMC-PCCF is more prone to cause instability, which can be avoided by optimizing system parameters and adding additional damping controls as the in-depth study of this article. Besides, the proposed design-oriented stability analysis method and the new sight at damping control is not limited to the MMC-PCCF-based HVdc system but are equally applicable for any other dc systems with dc-voltage-controlled converters.

Acknowledgment

The authors would like to thank Y. Tu and Y. Liu for their kind supports and wise advice. They would also like to thank H. Liu for his experimental supports.

References

[1] S. Dehnath, J. Qin, B. Bahrani, M. Saeedifard, and P. Barbosa, "Operation, control, and applications of the modular multilevel converter: A review," *IEEE Trans. Power Electron.*, vol. 30, no. 1, pp. 37–53, Jan. 2015.

[2] A. Lesnicar and R. Marquardt, "An innovative modular multilevel converter topology suitable for a wide power range," in *Proc. IEEE Power Tech Conf.*, Bologna, Italy, Jun. 2003, pp. 6–12.

[3] B. Li, Z. Xu, S. Shi, D. Xu, and W. Wang, "Comparative study of the active and passive circulating current suppression methods for modular multilevel converters," *IEEE Trans. Power Electron.*, vol. 33, no. 3, pp. 1878–1883, Mar. 2018.

[4] B. Jacobson, P. Karlsson, G. Asplund, L. Harbefors, and T. Jonsson, "VSC-HVDC transmission with cascaded two-level converters," in *Proc. CIGRE*, Paris, France, 2010, pp. B4–B110.

[5] Z. Xu, Y. Xue, and Z. Zhang, "VSC-HVDC technology suitable for bulk power overhead line transmission," (in Chinese), *Proc. CSEE*, vol. 34, no. 29, pp. 5051–5062, Oct. 2014.

[6] J. Sun, "Impedance-based stability criterion for grid connected inverters," *IEEE Trans. Power Electron. Lett.*, vol. 26, no. 11, pp. 3075–3078, Nov. 2011.

[7] S. Shah and L. Parsa, "Impedance modeling of three-phase voltage source converters in dq, sequence, and phasor domains," *IEEE Trans. Energy Convers.*, vol. 32, no. 3, pp. 1139–1150, Sep. 2017.

[8] X. Wang and F. Blaabjerg, "Harmonic stability in power electronic-based power systems: Concept, modeling, and analysis," *IEEE Trans. Smart Grid*, vol. 10, no. 3, pp. 2858–2870, May 2019.

[9] J. Sun, "Small-signal methods for AC distributed power system–A review," *IEEE Trans. Power Electron.*, vol. 24, no. 11, pp. 2545–2554, Nov. 2009.

[10] J. Lyu, X. Zhang, J. Huang, J. Zhang, and X. Cai, "Comparison of harmonic linearization and harmonic state space methods for impedance modeling of modular multilevel converter," in *Proc. Int. Power Electron. Conf.*, May 2018, pp. 1004–1009.

[11] J. Lyu, X. Zhang, X. Cai, and M. Molinas, "Harmonic state-space based small-signal impedance modeling of modular multilevel converter with consideration of internal harmonic dynamics," *IEEE Trans. Power Electron.*, vol. 34, no. 3, pp. 2134–2148, Mar. 2018.

[12] J. Lyu, X. Cai, and M. Molinas, "Optimal design of controller parameters for improving the stability of MMC-HVDC for wind farm integration," *IEEE J. Emerg. Sel. Topics Power Electron.*, vol. 6, no. 1, pp. 40–53, Mar. 2018.

[13] Z. Xu *et al.*, "A complete HSS-based impedance model of MMC considering grid impedance coupling," *IEEE Trans. Power Electron.*, vol. 35, no. 12, pp. 12929–12948, Dec. 2020.
[14] Z. Xu, B. Li, S. Wang, S. Zhang, and D. Xu, "Generalized single-phase harmonic state space modeling of the modular multilevel converter with zero-sequence voltage compensation," *IEEE Trans. Ind. Electron.*, vol. 66, no. 8, pp. 6416–6426, Aug. 2020.
[15] J. Sun and H. Liu, "Impedance modeling and analysis of modular multilevel converters," in *Proc. IEEE 17th Workshop Control Model. Power Electron.*, Jun. 2016, pp. 1–9.
[16] J. Sun and H. Liu, "Sequence impedance modeling of modular multilevel converters," *IEEE J. Emerg. Sel. Topics Power Electron.*, vol. 5, no. 4, pp. 1427–1443, Dec. 2017.
[17] L. Bessegato, L. Harnefors, K. Ilves, and S. Norrga, "A method for the calculation of the AC-side admittance of a modular multilevel converter," *IEEE Trans. Power Electron.*, vol. 34, no. 5, pp. 4161–4172, May 2019.
[18] L. Bessegato, K. Ilves, L. Harnefors, and S. Norrga, "Effects of control on the AC-side admittance of a modular multilevel converter," *IEEE Trans. Power Electron.*, vol. 34, no. 8, pp. 7206–7220, Aug. 2019.
[19] T. Yin *et al.*, "Impedance-based stability analysis and stabilization control strategy of MMC-HVDC considering complete control loops," *IEEE Access*, vol. 8, pp. 142900–142915, 2020.
[20] T. Yin *et al.*, "Modeling and analysis of high-frequency MMC impedance considering different control modes and voltage feedforward," *IEEE Access*, vol. 8, pp. 218575–218584, 2020.
[21] H. Wu, X. Wang, Ł. Kocewiak, and L. Harnefors, "AC impedance modeling of modular multilevel converters and two-level voltage-source converters: Similarities and differences," in *Proc. IEEE 19th Workshop Control Model. Power Electron.*, Jun. 2018, pp. 1–8.
[22] H. Wu and X. Wang, "Dynamic impact of zero-sequence circulating current on modular multilevel converters: Complex-valued AC impedance modeling and analysis," *IEEE J. Emerg. Sel. Topics Power Electron.*, vol. 8, no. 2, pp. 1947–1963, Jun. 2020.
[23] H. Wu, X. Wang, and Ł. Kocewiak, "Impedance-based stability analysis of voltage-controlled MMCs feeding linear AC systems," *IEEE J. Emerg. Sel. Topics Power Electron.*, vol. 8, no. 4, pp. 4060–4074, Dec. 2020.
[24] A. Cupertino, J. Farias, H. Pereira, S. Seleme, and R. Teodorescu, "Comparison of DSCC and SDBC modular multilevel converters for STATCOM application during negative sequence compensation," *IEEE Trans. Ind. Electron.*, vol. 66, no. 3, pp. 2302–2312, Mar. 2019.
[25] B. Li, L. Han, S. Mao, S. Zhou, Z. Qu, and D. Xu, "Decoupled modulation scheme for modular multilevel converters in medium-voltage applications," *IEEE Trans. Power Electron.*, vol. 35, no. 11, pp. 11430–11441, Nov. 2020.
[26] A. Cupertino, H. Pereira, S. Seleme, and R. Teodorescu, "On inherent redundancy of MMC-Based STATCOMs in the overmodulation region," *IEEE Trans. Power Del.*, vol. 35, no. 3, pp. 1169–1179, Jun. 2020.
[27] J. Peralta, H. Saad, S. Dennetiere, J. Mahseredjian, and S. Nguefeu, "Detailed and averaged models for a 401-level MMC-HVDC system," *IEEE Trans. Power Del.*, vol. 27, no. 3, pp. 1501–1508, Jul. 2012.
[28] A. Nami, J. Liang, F. Dijkhuizen, and G. D. Demetriades, "Modular multilevel converters for HVDC applications: Review on converter cells and functionalities," *IEEE Trans. Power Electron.*, vol. 30, no. 1, pp. 18–36, Jan. 2015.
[29] B. Zhang and H. Nademi, "Modeling and harmonic stability of MMC-HVDC with passive circulating current filters," *IEEE Access*, vol. 8, pp. 129372–129386, 2020.
[30] K. Ji, G. Tang, J. Yang, Y. Li, and D. Liu, "Harmonic stability analysis of MMC-Based DC system using DC impedance model," *IEEE J. Emerg. Sel. Topics Power Electron.*, vol. 8, no. 2, pp. 1152–1163, Jun. 2020.
[31] K. Ji, G. Tang, H. Pang, and J. Yang, "Impedance modeling and analysis of MMC-HVDC for offshore wind farm integration," *IEEE Trans. Power Del.*, vol. 35, no. 3, pp. 1488–1501, Jun. 2020.
[32] K. Ji, H. Pang, J. Yang, and G. Tang, "DC side harmonic resonance analysis of MMC-HVDC considering wind farm integration," *IEEE Trans. Power Del.*, vol. 36, no. 1, pp. 254–266, Feb. 2021.
[33] K. Ji *et al.*, "Generalized impedance analysis and new sight at damping controls for wind farm connected MMC-HVdc," *IEEE J. Emerg. Sel. Topics Power Electron.*, vol. 9, no. 6, pp. 7278–7295, Dec. 2021.
[34] Z. Li *et al.*, "Accurate impedance modeling and control strategy for improving the stability of DC system in multiterminal MMC-based DC grid," *IEEE Trans. Power Electron.*, vol. 35, no. 10, pp. 10026–10049, Oct. 2020.
[35] M. Nahalparvari, M. Asoodar, L. Bessegato, S. Norrga, and H. Nee, "Modeling and shaping of the DC-Side admittance of a modular multilevel converter under closed-loop voltage control," *IEEE Trans. Power Electron.*, vol. 36, no. 6, pp. 7294–7306, Jun. 2021.
[36] L. Harnefors, A. Antonopoulos, S. Norrga, L. Angquist, and H. Nee, "Dynamic analysis of modular multilevel converters," *IEEE Trans. Ind. Electron.*, vol. 60, no. 7, pp. 2526–2537, Jul. 2013.
[37] K. Ilves, A. Antonopoulos, S. Norrga, and H. P. Nee, "Steady-state analysis of interaction between harmonic components of arm and line quantities of modular multilevel converters," *IEEE Trans. Power Electron.*, vol. 27, no. 1, pp. 57–68, Jan. 2012.
[38] G. Bergna-Diaz, J. Freytes, X. Guillaud, S. D'Arco, and J. A. Suul, "Generalized voltage-based state-space modeling of modular multilevel converters with constant equilibrium in steady-state," *IEEE J. Emerg. Sel. Topics Power Electron.*, vol. 6, no. 2, pp. 707–725, Jun. 2018.
[39] A. Jamshidifar and D. Jovcic, "Small-signal dynamic DQ model of modular multilevel converter for system studies," *IEEE Trans. Power Del.*, vol. 31, no. 1, pp. 191–199, Feb. 2016.
[40] T. Li, A. M. Gole, and C. Zhao, "Harmonic instability in MMC-HVDC converters resulting from internal dynamics," *IEEE Trans. Power Del.*, vol. 31, no. 4, pp. 1738–1747, Aug. 2016.
[41] H. K. Nam, Y. K. Kim, K. S. Shim, and K. Y. Lee, "A new eigen-sensitivity theory of augmented matrix and its applications to power system stability," *IEEE Trans. Power Syst.*, vol. 15, no. 1, pp. 363–369, Feb. 2000.
[42] K. W. Wang and C. Y. Chung, "Multimachine eigenvalue sensitivities of power system parameters," *IEEE Trans. Power Syst.*, vol. 15, no. 2, pp. 741–747, May 2000.
[43] P. Ju *et al.*, "Frequency-domain sensitivity with application to power system modeling," *Proc. CSEE*, vol. 30, no. 28, pp. 19–24, Oct. 2010.
[44] D. Yang, X. Wang, M. Ndreko, and W. Winter, "Multi-frequency state-space model of MMC-HVDC system for design-oriented stability analysis," in *Proc. IEEE 9th Int. Power Electron. Motion Control Conf.*, Dec. 2020, pp. 961–965.
[45] J. Freytes *et al.*, "Improving small-signal stability of an MMC with CCSC by control of the internally stored energy," *IEEE Trans. Power Del.*, vol. 33, no. 1, pp. 429–439, Feb. 2018.
[46] Y. Li *et al.*, "Modeling and damping control of modular multilevel converter based DC grid," *IEEE Trans. Power Syst.*, vol. 33, no. 1, pp. 723–735, Jun. 2018.
[47] P. Li *et al.*, "Effects of control on the DC impedance of modular multilevel converters," in *Proc. 4th Int. Conf. HVDC*, Nov. 2020, pp. 595–601.
[48] Y. Li, J. Li, H. Xiao, J. Zhang, and Z. Du, "Stability analysis of droop-based converter using SISO method from DC side perturbation," *IEEE Trans. Power Del.*, vol. 36, no. 5, pp. 3150–3161, Oct. 2021.
[49] J. Bei *et al.*, "Coordinated flexible damping mechanism with inertia emulation capability for MMC-MTDC transmission systems," *IEEE J. Emerg. Sel. Topics Power Electron.*, vol. 9, no. 6, pp. 7329–7342, Dec. 2021.
[50] J. Beerten, S. D'Arco, and J. A. Suul, "Frequency-dependent cable modelling for small-signal stability analysis of VSC-HVDC systems," *IET Gener., Transmiss. Distrib.*, vol. 10, no. 6, pp. 1370–1381, 2016.
[51] L. Harnefors, X. Wang, A. G. Yepes, and F. Blaabjerg, "Passivity based stability assessment of grid-connected VSCs–An overview," *IEEE J. Emer. Sel. Topics Power Electron.*, vol. 4, no. 1, pp. 116–125, Mar. 2016.
[52] H. Gong, X. Wang, L. Harnefors J. Hasler, and C. Danielsson, "Admittance-dissipativity analysis and shaping of dual-sequence current control for VSCs," *IEEE J. Emerg. Sel. Topics Power Electron.*, to be published, doi: 10.1109/JESTPE.2021.3067553.

Pengkun Li (Graduate Student Member, IEEE) received the B.S. degree in electrical engineering from Beijing Jiaotong University, Beijing, China, in 2017. He is currently working toward the Ph.D. degree with Xi'an Jiaotong University, Xi'an, China.

His research interests include modeling, control, and small-signal harmonic stability analysis of power electronic-based power systems.

Yue Wang (Member, IEEE) was born in Liaoning, China, in 1972. He received the B.S. degree from Xi'an Jiaotong University, Xi'an, China, in 1994, the M.S. degree from Beijing Jiaotong University, Beijing, China, in 2000, and the Ph.D. degree from Xi'an Jiaotong University, Xi'an, China, in 2003, all in electrical engineering.

He is currently a Full Professor with the School of Electrical Engineering, Xi'an Jiaotong University. His research interests include wireless power transfer, active power filters, multilevel converters, and HVdc.

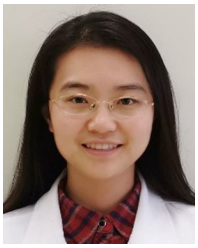

Xuan Li (Member, IEEE) was born in Jiangsu, China, in 1989. She received the B.S. degree from Xi'an Jiaotong University, Shaanxi, China, in 2011, and the M.S. degree from Tsinghua University, Beijing, China, in 2013.

She is currently a Senior Engineer with State Grid Economic and Technological Research Institute, Beijing, China. Her main research interests include VSC-HVdc and LCC-HVdc system design, as well as renewable energy integration.

Bo Yue was born in Shaanxi, China, in 1976. He received the Ph.D. degree in electrical engineering from Xi'an Jiaotong University, Xi'an, China, in 2003.

He is currently a Senior Engineer with State Grid Economic and Technological Research Institute Co., Ltd., Beijing, China. His main research interests include HVdc and high voltage technology.

Runtian Li was born in Hebei, China, in 1998. He received the B.S. degree in electrical engineering from Southwest Jiaotong University, Chengdu, China, in 2020. He is currently working toward the M.S. degree with Xi'an Jiaotong University, Xi'an, China.

His research interests include MMC-HVdc, power quality, and the applications of power electronics in power systems.

Bole Feng received the B.S. degree in electrical engineering and automation from the Guangdong University of Technology, Guangzhou, China, in 2020. He is currently working toward the M.S. degree in electrical engineering with Xi'an Jiaotong University, Xi'an, China.

His research interests include the modeling and control of modular multilevel converters and HVdc.

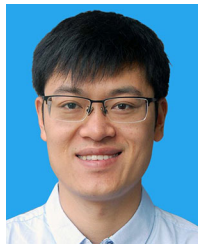

Taiyuan Yin is currently working toward the Ph.D. degree in electrical engineering with Xi'an Jiaotong University, Xi'an, China.

His current interests include modeling and control of modular multilevel converters and stability analysis of MMC-based HVdc systems.